

RESEARCH ARTICLE | SEPTEMBER 25 2024

## Molecular dynamics of quantitative evaluation of confined fluid behavior in nanopores media and the influencing mechanism: Pore size and pore geometry

Rixin Zhao ; Haitao Xue; Shuangfang Lu  ; H. Chris Greenwell ; Yaohui Xu; Taohua He; Valentina Erastova  



*Physics of Fluids* 36, 092027 (2024)

<https://doi.org/10.1063/5.0226864>



### Articles You May Be Interested In

Investigation of oil/water two-phase flow behavior in laminated shale porous media considering heterogeneous structure and fluid-solid interaction

*Physics of Fluids* (March 2024)

Extending van der Waals equation of state by molecular potential theory to study nano-confined gas properties

*Physics of Fluids* (September 2024)

Permeability prediction of considering organic matter distribution based on deep learning

*Physics of Fluids* (March 2023)



Physics of Fluids

Special Topics Open  
for Submissions

[Learn More](#)

# Molecular dynamics of quantitative evaluation of confined fluid behavior in nanopores media and the influencing mechanism: Pore size and pore geometry

Cite as: Phys. Fluids **36**, 092027 (2024); doi: 10.1063/5.0226864

Submitted: 4 July 2024 · Accepted: 5 September 2024 ·

Published Online: 25 September 2024



View Online



Export Citation



CrossMark

Rixin Zhao,<sup>1,2,3</sup> Haitao Xue,<sup>4</sup> Shuangfang Lu,<sup>5,a)</sup> H. Chris Greenwell,<sup>3</sup> Yaohui Xu,<sup>1,2</sup> Taohua He,<sup>1,2</sup> and Valentina Erastova<sup>6,a)</sup>

## AFFILIATIONS

<sup>1</sup>College of Resources and Environment, Yangtze University, Wuhan, Hubei 430100, China

<sup>2</sup>Hubei Key Laboratory of Petroleum Geochemistry and Environment, Yangtze University, Wuhan, Hubei 430100, China

<sup>3</sup>Department of Earth Sciences and Department of Chemistry, Durham University, Durham DH1 3LE, United Kingdom

<sup>4</sup>School of Geosciences, China University of Petroleum (East China), Qingdao, 266580 Shandong, China

<sup>5</sup>Sanya Offshore Oil & Gas Research Institute, Northeast Petroleum University, Sanya 572025, China

<sup>6</sup>School of Chemistry, University of Edinburgh, David Brewster Road, Edinburgh EH9 3FJ, United Kingdom

<sup>a)</sup> Authors to whom correspondence should be addressed: [846043531@qq.com](mailto:846043531@qq.com) and [valentina.erastova@ed.ac.uk](mailto:valentina.erastova@ed.ac.uk)

## ABSTRACT

Understanding the potential mechanisms of reservoir fluid storage, transport, and oil recovery in shale matrices requires an accurate and quantitative evaluation of the fluid behavior and phase state characteristics of the confined fluid in nanopores as well as the elucidation of the mechanisms within complex pore structures. The research to date has preliminary focused on the fluid behavior and its influencing factors within a single nanopore morphology, with limited attention of the role of pore structures in controlling fluid behavior and a lack of quantitative methods for characterizing the phase state of fluids. To address this gap, we utilize molecular dynamics simulations to examine the phase state characteristics of confined fluids across various pore sizes and geometries, revealing the mechanisms by which wall boundary conditions influence fluid behavior. We use the simulation results to validate the accuracy and applicability of the quantitative characterization model for fluid phase state properties. Our findings show that the phase state features of fluids differ significantly between slit-like and cylindrical pores, with lower adsorption limits in pore sizes of 2.8 and 7 nm, respectively. Based on pore sizes, we identified three regions of confined fluid phases and determined that the influence of the adsorbed state fraction on fluid phase state cannot be ignored for pores smaller than approximately 85 nm. Additionally, cylindrical pores interact with the internal fluids about 1.8 times stronger than slit-like pores.

© 2024 Author(s). All article content, except where otherwise noted, is licensed under a Creative Commons Attribution-NonCommercial 4.0 International (CC BY-NC) license (<https://creativecommons.org/licenses/by-nc/4.0/>). <https://doi.org/10.1063/5.0226864>

## NOMENCLATURE

$A_m$	Pore specific surface area, $\text{nm}^2$	$Q_a$	Adsorption amount per unit weight rock, $\text{mg/g}$
$c_a$	Adsorption capacity per unit area, $\text{mg/m}^2$	$Q_f$	Free amount per unit weight rock, $\text{mg/g}$
$d_m$	Pore diameter, $\text{nm}$	$r_{\text{acyl}}$	Mass ratio of fluid adsorbed within a cylindrical pore with given diameter, %
$F$	Correction coefficient for pore geometry, dimensionless	$r_{\text{am}}$	Mass ratio of fluid adsorbed within a pore with given diameter, %
$H$	Mean adsorption thickness, $\text{nm}$	$r_{\text{asli}}$	Mass ratio of fluid adsorbed within a slit-like pore with given diameter, %
$n$	Mean adsorption layer number in pores coexisting with the adsorbed and free phases, dimensionless		

$r_{\text{asph}}$	Mass ratio of fluid adsorbed within a spherical pore with given diameter, %
$t_{\text{ai}}$	Mean monolayer adsorption thickness, nm
$\rho_a$	Mean density of adsorbed phase in pores, $\text{kg}/\text{m}^3$
$\rho_{\text{ali}}$	Mean density of the monolayer adsorption phase, $\text{kg}/\text{m}^3$
$\rho_f$	Mean density of bulk phase in pores, $\text{kg}/\text{m}^3$
$\rho_{\text{mass}}$	Mean mass density of the confined fluid within pores, $\text{kg}/\text{m}^3$
$\rho_{\text{num}}$	Mean number density of the confined fluid within pores, the number of molecules per cubic nanometer, $\text{nm}^{-3}$
$\sigma_{\text{df}}$	Discriminant function for adsorption layer number, dimensionless

## I. INTRODUCTION

Given the increasingly prominent contradiction between global energy consumption and insufficient supply, the development of shale oil reservoirs has garnered significant attention from both academic and industrial sectors, being considered key to ensuring resource security.<sup>1</sup> Over the past decade, the United States has become the world's foremost producer of crude oil, primarily through the effective exploitation of shale oil resources. In 2020, the production of marine shale oil reached  $747 \times 10^6$  tons.<sup>2</sup> Inspired by the success of North American shale oil development, shale reservoirs have attracted extensive interest across the sector, emerging as a central area of inquiry in the unconventional oil and gas domain.<sup>3–5</sup> Although the scale of shale oil exploration and development continues to expand, significant challenges persist, including low production from individual wells and a rapid decline in output, making efficient development difficult. Recent research indicates that nanoporous networks composed of clay minerals and spongy organic matter (OM) pores within organic-rich shales constitute the primary storage spaces for fluids in shale reservoirs.<sup>6</sup> Within the nanoscale pore network of shale, fluid–solid interactions induce oil to exhibit different phase states (adsorbed and free states). Nevertheless, inappropriate descriptions of the microscale confined fluid phases and insufficient comprehension of the micro-mechanisms can lead to inaccuracies in the assessment of shale oil reserves and mobility. Therefore, a comprehensive understanding of the behavior of nanoscale confined fluids in shale reservoirs is imperative for the exploration and efficient development of shale oil.

It is observed that shale exhibits a wide range of pore sizes—from nanometer-scale micropores to micrometer-scale or even larger macropores and microfractures—and complex, heterogeneous geometries, forming both connected and disconnected local pore domain structures.<sup>7,8</sup> Fluids confined within nanoscale pores exhibit complex behaviors due to fluid–solid interactions, exceeding the behavior of bulk phase fluids in larger pores. Although current studies have conducted experimental research utilizing nanomaterials with specific pore geometries, the behavior characteristics of nanoconfined fluids and the precise determination of the lower limit of pore size for adsorption states fluid still require further investigation.<sup>9</sup> Given the constraints imposed by the nanoscale, the preparation of nanoscale experimental setups is not only time-consuming and expensive, but accurately observing and measuring the behavior and flow of confined fluids in synthetic nanoscale pore materials remains challenging. As a result, relatively few experimental studies have been reported on the behavior of confined fluids within the complex geometric pore networks of shale at the microscale.<sup>10,11</sup>

In the typical lacustrine shale formations of China, there is a prevalent presence of clay minerals, such as montmorillonite, illite, and kaolinite, with high concentrations typically reaching between 5 and 55%.<sup>6</sup> These clay minerals are characterized by fine granularity, a large specific surface area (approximately  $800 \text{ m}^2/\text{g}$ ), and high chemical reactivity at surface defect sites, which significantly enhances their adsorption capabilities for metal ions and organic molecules.<sup>12,13</sup> Although the clay minerals in shale reservoirs are predominantly composed of illite and illite/smectite mixed layers, rock x-ray diffraction analysis has revealed that the kaolinite content in certain continental shales is also considerably high, comprising up to 28% of the total clay content (Fig. S1, [supplementary material](#)). Kaolinite does not feature isomorphous substitutions, like montmorillonite or illite, and as a result, it does not have a permanent negative charge, and it does not swell.<sup>14</sup> However, unlike other clay minerals, kaolinite features two surfaces—one hydrophobic siloxane and another hydrophilic hydroxide. These properties make kaolinite a unique and important contributor to the formation, migration, and enrichment of shale oil.<sup>15</sup> On the other hand, the spongy pores within organic matter in shale constitute another important hydrocarbon fluid storage space.<sup>16</sup> Therefore, investigating the fluid behavior and adsorption mechanisms of organic hydrocarbon molecules within the pore spaces of both clay minerals and organic matter is key for elucidating the fluid distribution patterns in shale reservoirs.

Pores comparable in size to the mean free path of fluid molecules significantly affect the free thermal motion of the molecules, leading to distinct behaviors and thermodynamic properties of confined fluids as opposed to those of bulk phase fluids in larger pores.<sup>17–19</sup> These factors induce notable deviations in the behavior characteristics of fluids in nanopores from those in bulk phases, primarily manifesting as uneven density distributions of confined fluids,<sup>20,21</sup> modifications in critical properties and saturation points,<sup>22,23</sup> reduced surface tension,<sup>24,25</sup> and decreased fluid viscosity.<sup>26,27</sup> The phase state characteristics of fluids in pores depend on the fugacity of fluid components in each phase, assessed through phase equilibrium calculations typically derived from equations of state (EOS). Thus, the accuracy of the EOS is crucial for precisely assessing fluid phase state characteristics. Given the significant deviations in the behavior of confined fluids compared to bulk phases, modifications to the form or application methods of EOS are necessary. Recently, several studies considering fluid–solid interactions have proposed modified EOS to calculate the phase state characteristics of fluids confined by pore size.<sup>28–30</sup> Research indicates that as the pore radius approaches infinity, all modified EOS simplify to classical EOS expressions, suggesting that under large pore conditions, the phase behavior of confined fluids aligns with that of bulk phase fluids.<sup>31</sup> However, classical van der Waals theory-based methods previously assumed a uniform confined fluid density and introduced an expression derived from maximum enclosure constraints to evaluate pore size effects, contradicting the actual non-uniform density distributions caused by fluid–solid interactions, failing to accurately reflect the phase state characteristics of nanoconfined fluids under small pore conditions. Moreover, using these modified EOS to simulate the behavior of nanoconfined fluids in heterogeneous shales is challenging to validate against molecular simulation results or experimental data.<sup>32</sup> When constructing equations to describe fluid phase state characteristics, factors such as differences in fluid–solid interactions, pore size distribution, and the geometric shapes of different pores in shale should be

considered. As pore size increases, the behavior characteristics of nanoconfined fluids gradually transition to those of bulk phase fluids, emphasizing the importance of determining the pore size limit that influences the behavior of confined fluids due to fluid–solid interactions. Recently, some researchers have proposed quantitative equations based on the theoretical derivation and volumetric methods to describe the behavior characteristics of nanoconfined fluids, but key parameters in existing models, such as adsorption thickness and the densities of adsorbed and free states of fluids, are often difficult to obtain experimentally.<sup>33</sup> At the same time, verifying the fairness of these theoretical equations within pores of different sizes and geometries remains a challenge.<sup>30,34,35</sup> Therefore, it is imperative to develop a quantitative equation that accounts for fluid–solid interactions to describe the behavior and phase state characteristics of confined fluids in nanopores, and to elucidate the mechanisms of influence by pore size and pore geometry.

Molecular dynamics (MD) simulation methods are considered an effective bridge between experimental phenomena and microscopic mechanisms due to their ability to provide atomistic details to chemophysical processes.<sup>36</sup> These methods provide an alternative approach to study complex fluid–solid interactions at the nanoscale and offer molecular-scale insights into their mechanisms of action.<sup>37,38</sup> Researchers have employed MD simulations to investigate the behavior and adsorption characteristics of fluids in nanoconfined pores. Existing studies have predominantly concentrated on the effects of individual factors such as fluid components,<sup>39,40</sup> external environments,<sup>41</sup> water content,<sup>42</sup> and ion types,<sup>37,43,44</sup> but there are fewer systematic studies on the impact of pore size and geometry differences in nanopores on fluid behavior. Moreover, due to challenges in constructing complex models of solid walls interacting with organic hydrocarbons, there is limited research on how differences in pore wall properties and reservoir space structures affect the behavior of nanoconfined fluids. The limitations of existing simulation studies include the following: (i) The analysis of fluid–solid interactions is generally based on qualitative assessments of molecular configurations and density distributions, without employing quantitative methods to evaluate the behavior of nanoconfined fluids. (ii) The substantial heterogeneity of shale reservoir has seldom been systematically examined in prior research, particularly concerning the impact of nanopore size distribution and varying pore geometries on the confined fluid behavior, phase characteristics, and underlying microscopic mechanisms.

In this study, MD simulations were conducted to investigate the adsorption behavior and microscopic mechanisms of interactions of hydrocarbons within kaolinite pores and organic matter pores, each characterized by distinct pore size distributions and geometries, thereby addressing the limitations of prior research. We constructed models of kaolinite slit pores with two (hydrophilic and hydrophobic) exposed surfaces and organic carbon nanotube cylindrical pores with a distribution of pore sizes. The primary objectives of this work are (i) to quantify the adsorption behavior and interaction strengths between the surfaces of kaolinite and carbon nanotubes and organic hydrocarbon fluids; (ii) to elucidate the effects of pore size distribution and geometries of shale matrix pores on the behavior and phase state characteristics of nanoconfined fluids; and (iii) to develop a mathematical model based on MD simulations that accounts for the differences in fluid–solid interactions, pore size distributions, and the variations in

geometries of different pores in shale, validating this model against theoretical and volumetric methods.

## II. METHODOLOGY

### A. Quantitative estimation method of different phase states content of confined fluid

#### 1. Basic theory and assumption

Notwithstanding the complexity of shale pore structures, homogeneous pore configurations are frequently presumed in the course of quantitative computations and model development.<sup>34</sup> For example, when performing quantitative pore structure characterization experiments such as mercury injection capillary pressure or nitrogen adsorption tests to calculate the pore size distribution of shale, the pores are frequently regarded as spherical pores to calculate the pore size by pore volume,<sup>45,46</sup> and in fluid flow modeling, spherical or cylindrical pores are frequently employed as boundary conditions to analyze fluid flow characteristics.<sup>30</sup> Song and Chen *et al.* studied the Poiseuille flow characteristics of simple fluids by simplification of the pores into cylindrical and slit-like pores and found that there is no appreciable difference between the fluid density distributions in different pore shapes when flow–wall interaction is ignored.<sup>47</sup> However, when flow–wall interaction is taken into account, cylindrical pores have a higher fluid absorption capacity than slit-like pores. Therefore, in this study, we assumed that the predominant pore types of shale are slit-like pores developed in inorganic minerals and cylindrical pores developed in organic matter [Fig. 1(b)], and we developed a model to characterize the phase states of hydrocarbon fluids in various pore structures under the condition of flow–wall interaction.

Figure 1(a) depicts a shale matrix with a complex material composition in its macroscopic state, in which organic and inorganic minerals form a complex pore network and are distributed in a combination. Previous researchers examined the adsorption behavior of liquid alkanes in the nanoscale carbonaceous slits of shale using MD simulations and found that the interaction between the pore surface and the inner fluid is not negligible for the shale rich in nanopores.<sup>38,41,48</sup> The interaction between the pore walls and the fluid results in a non-uniform density distribution of the hydrocarbon fluids, and the fluid density distribution curve reveals a distinct multilayer adsorption feature [Fig. 1(c)]. Therefore, as illustrated in Fig. 1(b), the phase states of the fluid inside the pore are mostly formed of adsorbed and free states, as determined by the fluid's density distribution. Meanwhile, heavy alkanes, resins, and asphaltenes, which represent heavy components, are more likely to be adsorbed near the pores' walls, whereas light components and some aromatic hydrocarbons are free within the pores' inner region.<sup>49</sup> Based on the aforementioned theories and hypotheses, this study establishes a method for quantitatively evaluating the phase state characteristics of hydrocarbon fluids in shale based on MD simulations.

#### 2. Hydrocarbon fluid adsorption parameters calculation

In this study, the position of the adsorption layers along the pore walls—including the adsorption thickness and the number of adsorption layers—is determined by the heterogeneous distribution of hydrocarbon fluid density, which is affected by fluid–solid interactions within confined spaces [Fig. 1(c)]. The position of these adsorption

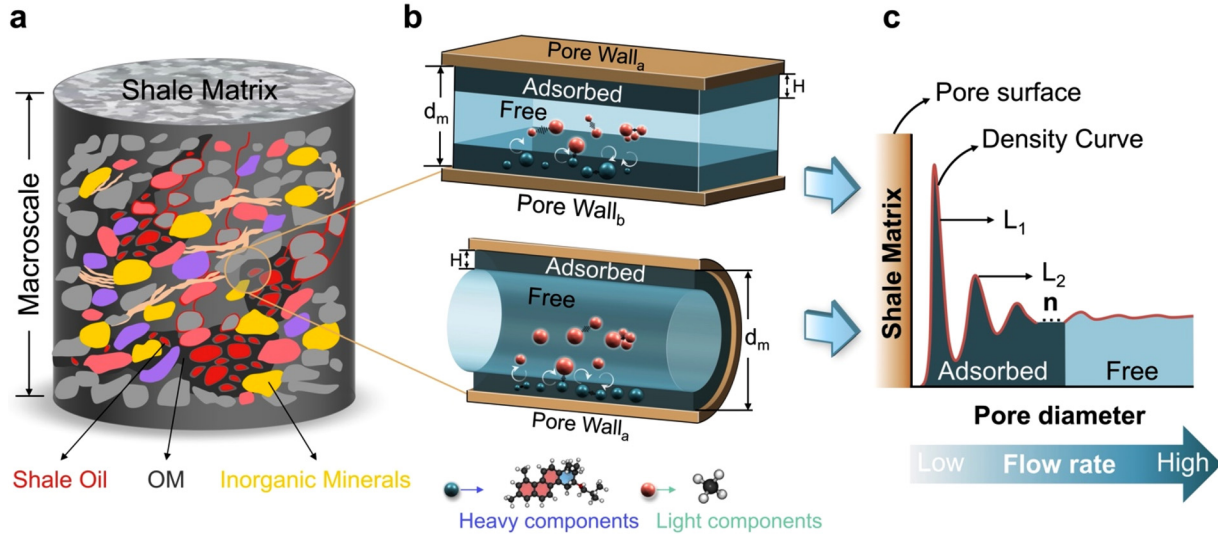


**FIG. 1.** (a) Schematic diagram of the macroscopic shale matrix, which contains a complex distribution of inorganic minerals, organic matter (OM), and hydrocarbon fluids; (b) regular slit-like pore and cylindrical pore model, with the dark component within the pore representing the adsorbed state and the light component representing free state fluids; and (c) density distribution curve of hydrocarbon fluids.

layers is crucial for calculating the adsorption parameters of hydrocarbon fluids. The calculation of the spatial density distribution of hydrocarbon fluids in this study is shown in Sec. 2.1 of the [supplementary material](#). To quantitatively assess the adsorption layer thickness, this study introduced a discriminant function,  $\sigma_{df}$  which is used to determine the position of the adsorption layer,

$$\sigma_{df} = \frac{\rho_{ali} - \rho_f}{\rho_f} \times 100\%, \quad (1)$$

where the  $\rho_{ali}$  and  $\rho_f$  in Eq. (1) are determined based on calculations from Eqs. (4) and (6) in the [supplementary material](#), utilizing data from the molecular number density distribution. A  $L_i$  layer is classified as an adsorption layer when the fluid density within  $L_i$  undergoes a fluctuation exceeding 2% compared to the bulk fluid density, that is, the discriminant function  $\sigma_{df} > 2\%$ .

Based on the determination of the position of the adsorption layers, the total adsorption thickness,  $H$ , of the hydrocarbon fluids can be expressed by the following equation:

$$H = \sum_{i=1}^n t_{ai}, \quad (2)$$

where  $t_{ai}$  is the monolayer adsorption thickness, in nm;  $n$  is the number of adsorption layers,  $i = 1, 2, \dots, n$ . Previous studies have indicated that the adsorption strength of organic hydrocarbon fluids by inorganic minerals (such as clay) and organic matter (such as kerogen) is primarily attributed to the surface area of the solid walls.<sup>50,51</sup> Given that simulations of liquid hydrocarbons rely on the bulk density to determine the number of molecules loaded, and considering the variability in molecule numbers across different systems, comparing their spatial density distributions can be challenging. Therefore, to more accurately represent the strength of interactions between the solid walls and the internal fluids, this study introduced the normalized density-

based adsorption per unit area,  $C_a$ , to characterize the adsorption capability of clay and organic matter walls toward organic hydrocarbon fluids,

$$C_a = \frac{m_a}{A_m} = \frac{\int_{L_i}^{L_{i+1}} A_m \cdot \rho_{mass} dL}{A_m}, \quad (3)$$

where  $A_m$  is the area of the solid wall surface, in  $m^2$ ;  $m_a$  is the mass of adsorbed molecules, in mg;  $C_a$  is the amount of adsorption per unit area,  $mg/m^2$ .

### 3. Quantitative characterization model of different phase states of hydrocarbon fluids

Based on Eq. (3), the adsorption quantity per unit area of a specific solid wall for a confined fluid can be determined, enabling the calculation of the fluid's adsorption amount  $Q_a$  as follows:

$$Q_a = A_p \cdot (C_a + C_b), \quad (4)$$

where  $C_a$  and  $C_b$  represent the adsorption per unit area of different pore walls in the slit-like pore, in  $mg/m^2$ , respectively. The free amount of fluid in the pore at a given diameter can be determined using the density of the fluid in its free state,

$$Q_f = \rho_f \cdot V_f = \rho_f \cdot A_p (d_m - 2H), \quad (5)$$

where  $d_m$  is the pore diameter, in nm. From Eqs. (4) and (5), the mass ratio of fluid adsorbed in a pore of a certain diameter can be determined as

$$r_{asli} = \frac{Q_a}{Q_a + Q_f} = \frac{C_a + C_b}{(C_a + C_b) + \rho_f \cdot (d_m - 2H)}. \quad (6)$$

Assuming that the interaction between these two walls of the slit-like pore for the internal fluid is identical, with  $C_a = C_b$ , the adsorbed mass ratio  $r_{asli}$  can be calculated as

$$r_{asli} = \frac{Q_a}{Q_a + Q_f} = \frac{2C_a}{2C_a + \rho_f \cdot (d_m - 2H)}. \quad (7)$$

Building on the conclusions from previous research that the interaction between solid pore walls and internal fluids is primarily associated with the wall's surface area,<sup>52</sup> it has been determined that slit pores exhibit the same adsorption per unit area as cylindrical and spherical pores.<sup>47</sup> Therefore, Eq. (7) can be extended to express the adsorption mass ratio of fluids within cylindrical and spherical pores of a specific diameter as follows:

$$\begin{aligned} r_{acyl} &= \frac{2C_a \cdot \pi r_m h_p}{2C_a \cdot \pi r_m h_p + \rho_f \cdot \pi (r_m - H)^2 h_p} \\ &= \frac{4d_m \cdot C_a}{4d_m \cdot C_a + \rho_f \cdot (d_m - 2H)^2}, \quad (8) \\ r_{asph} &= \frac{4C_a \cdot \pi r_m^2}{4C_a \cdot \pi r_m^2 + \rho_f \cdot \frac{4}{3} \pi (r_m - H)^3} = \frac{6d_m^2 \cdot C_a}{6d_m^2 \cdot C_a + \rho_f \cdot (d_m - 2H)^3}. \quad (9) \end{aligned}$$

Combining Eqs. (7)–(9) allows for the consolidation of the adsorption mass ratio of fluids within pores of a given diameter into a unified equation that quantitatively characterizes the different phase state characteristics of hydrocarbon fluids. This unified equation can be expressed as follows:

$$r_{am} = \frac{2FC_a \cdot d_m^{F-1}}{2FC_a \cdot d_m^{F-1} + \rho_f \cdot (d_m - 2H)^F}, \quad (10)$$

where  $d_m \geq 2H$ . As  $d_m > 2H$ , it can be deduced that  $0 < r_{am} < 1$ , suggesting that the majority of fluids in the shale pores coexist in adsorbed and free states. When  $d_m = 2H$ , the pore space is completely occupied by adsorbed fluid and  $r_{am} = 1$ .  $F$  is the dimensionless corrections coefficient for pore shape, where  $F = 1, 2, \text{ or } 3$  for slit-like, cylindrical, and spherical pore geometries, respectively. By combining Eqs. (2) and (3), Eq. (10) can be used to estimate the adsorption mass ratio of fluid within a pore of a given diameter for various pore geometries. Based on the calculated adsorption mass ratio, the adsorption volume ratio of the fluid within the pore can be calculated as

$$r_{av} = \frac{V_a}{V_p} = \frac{r_{am} \cdot \rho_f}{r_{am} \cdot \rho_f + (1 - r_{am}) \cdot \rho_a}. \quad (11)$$

#### 4. The diffusion coefficients

Mean squared displacement (MSD) defines the particle displacement patterns within a system over time in dynamic simulations. Specifically, it assists in discerning whether particles are diffusing freely, transported, or restricted. The diffusion coefficient ( $D$ ) of the alkane molecule is based on the MSD determined from a coordinate file of molecular trajectories after system equilibrium and then calculated using Einstein's relation equation,

$$3D = \lim_{t \rightarrow \infty} \frac{1}{2t} \left\langle \frac{1}{N} \cdot \sum_{i=1}^N [r_i(t) - r_i(0)]^2 \right\rangle, \quad (12)$$

where  $3D$  represents the molecular diffusion coefficient in the three-dimensional direction;  $D$  is the diffusion coefficient,  $10^{-9} \text{ m}^2/\text{s}$ ;  $r_i(t)$  is the coordinate of  $i$  molecules at simulation time  $t$ ; and  $N$  is the total number of molecules in the system.

#### 5. Fluid-solid interaction energy

In the process of conducting MD simulations, we define energy groups to analyze the non-bonded interaction energies between hydrocarbon fluids and wall surfaces through a rerun of the trajectories. Typically, only non-bonded interactions including van der Waals forces (represented by the 12-6 Lennard-Jones potential) and long-range Coulomb interactions are considered, as depicted by Eq. (13). Initial simulations are conducted utilizing the particle mesh Ewald (PME) method for periodic dynamical investigations to ensure the accuracy of interaction energy computations. Subsequently, the cutoff approach is utilized to calculate electrostatic interactions. The designation of energy groups is followed by a rerun of the simulation trajectories,

$$E_{nonbond} = \sum_i E_i^{Coul} + \sum_{j>i} E_{ij}^{Coul} + \sum_i E_i^{VDW} + \sum_{j>i} E_{ij}^{VDW}, \quad (13)$$

where  $i$  and  $j > i$  represent non-bonded intramolecular and intermolecular interactions, respectively. This study focuses solely on the energies of intermolecular interactions, disregarding the intermolecular interactions energy component. In particular,  $E_{ij}^{Coul}$  and  $E_{ij}^{VDW}$  represent the long-range intermolecular Coulomb and van der Waals interaction terms, respectively.

#### B. Molecular models with distinct pore geometries and different pore diameters

In recent years, microscale image analyses of organic-rich shale pore structures using high-resolution characterization techniques such as field-emission scanning electron microscopy have revealed that the microscale pore architecture of shale is intricate,<sup>53</sup> developing highly inhomogeneous pore systems comprised of pores with different geometries, controlled primarily by the rich organic matter content and multiple mineral compositions, ranging in size from nanometers to micrometers.<sup>54</sup> Despite the complexity of the pore geometry of shales, previous research has determined that both marine and continental shales are dominated by slit-like and cylindrical pores.<sup>6,16,55</sup> Among them, slit-like pores are predominantly developed in inorganic minerals such as clay minerals [Fig. 2(a), top], forming a pore network with narrow, deformed slit-like pores that have been warped by burial extrusion. Cylindrical pores [Fig. 2(a), bottom] are predominant in organic materials (kerogen and asphaltene) and form a complicated pore-throat network with a large pore space and narrow throats (ink bottle-like). Therefore, in this study, slit and cylindrical pore models based on inorganic minerals and organic matter as matrix walls are constructed to evaluate the accuracy of the model and examine the mechanism of hydrocarbon fluids under the restrictions of varied pore diameters and pore geometries.

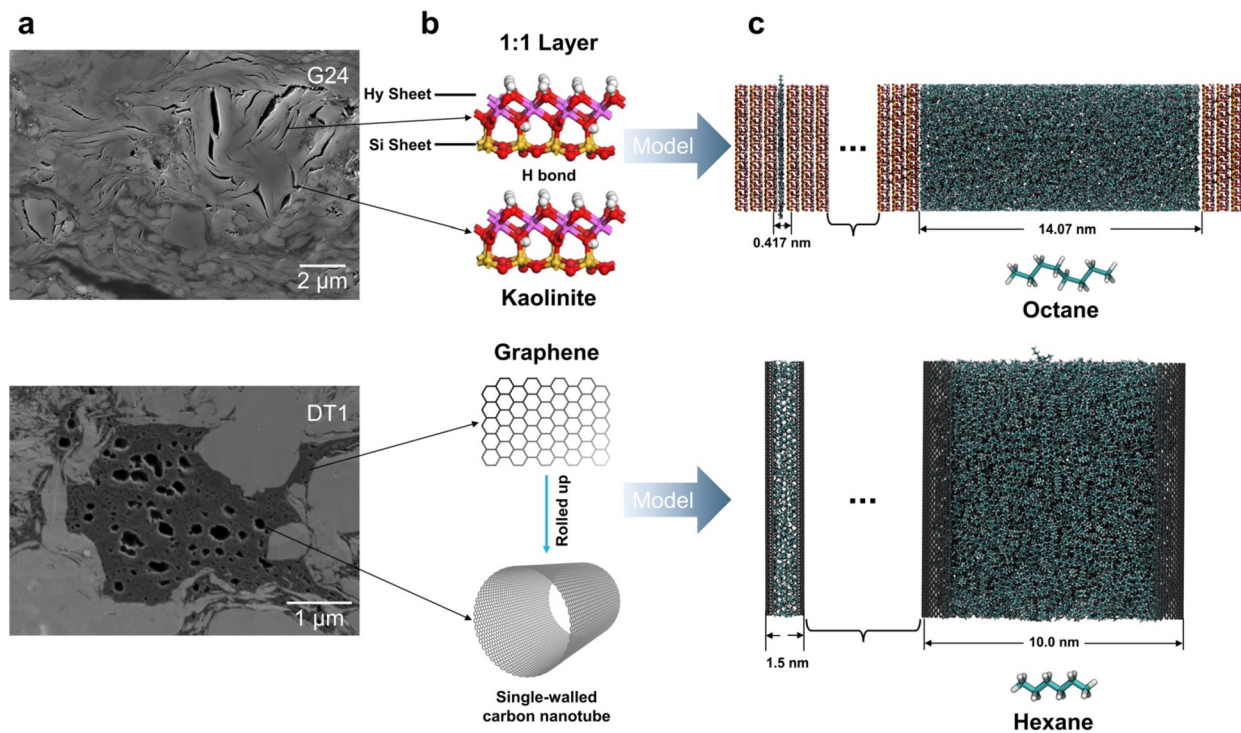


**FIG. 2.** Schematic diagram of molecular modeling of slit-like and cylindrical pores. (a) Slit-like pores formed by clay minerals (kaolinite) in continental shale and cylindrical pores developed within the organic matter (carbon nanotube) in marine shale captured by FE-SEM; (b) matrix cell model of clay minerals (top) and single-layer carbon nanotubes obtained by rolling graphene sheets (bottom); and (c) initial molecular model established in this manuscript includes slit-like pores of clay (top) with the octane system and cylindrical organic pores with the hexane system.

The process of molecular modeling of slit-like and cylindrical pores with varying pore diameters is depicted in Fig. 2. As indicated in the top of Fig. 2(b), the inorganic mineral matrix used for this paper is kaolinite, and the chemical formula of the kaolinite unit cell is  $\text{Al}_2\text{Si}_2\text{O}_5(\text{OH})_4$ , with the initial atomic coordinate positions obtained from the American Mineralogist Crystal Structure Database.<sup>56</sup> The periodic replication supercell consists of two adjacent kaolinite sheets, each of which is constructed of 252 unit cells ( $12 \times 7 \times 3$ ), with one side of the mineral wall measuring approximately  $6 \times 6 \times 2 \text{ nm}^3$ . In this research, pore diameters are modified by adjusting the number of fluid molecules within the pores under isothermal–isobaric ensemble conditions (NPT ensemble), and associated slit pore parameters such as pore diameter and molecule count can be found in the [supplementary material](#) (Table S1). Despite the reality that kaolinite is not a substantial component of the clay minerals in shale, the contact between this form of clay and hydrocarbon fluids happens predominantly on several sides of the particles or at the clay edges due to its unique 1:1 dioctahedral phyllosilicate properties of non-swelling clay mineral, which has minimal homogenous substitution and is not permanently charged. Therefore, the choice of kaolinite as an inorganic mineral matrix can limit the interference of surface charge and matrix swelling on the results of studying the effect of molecular pore diameter and pore geometry on the phase state of hydrocarbon fluid.<sup>57</sup> It is important to note that the upper and lower surfaces of kaolinite are quite distinct, with the oxygen atoms of its aluminum trihydrate class being typically terminated by oxygen atoms to form a layer of hydroxyl groups; hence

this class of aluminum trihydrate surfaces are called hydroxyl surface, while the siloxane tetrahedral surfaces are called siloxane surface [Fig. 2(a), top]. Due to electron polarization, although the overall net charge of the kaolinite cell is zero, the siloxane and hydroxyl surfaces have a slight net negative and positive charge, respectively (whereby this polarization is implicitly captured by the partial charges on each atom, according to the definition of the force field utilized in this paper).<sup>58,59</sup>

Carbon nanotubes generated by rolling graphene sheets were selected as the matrix walls of organic matter in this study [Fig. 2(b), bottom]. The molecular models of carbon nanotubes with different chirality were created using the Nanotube Builder plug-in in the VMD molecular visualization software,<sup>60</sup> and the molecular models of cylindrical pores with different pore diameters were created independently, while keeping the length of carbon nanotubes constant at 10 nm. Due to the rigid nature of carbon nanotubes, the NVT ensemble (isovolumetric isothermal ensemble) was selected for the simulation of cylindrical pores in this study. The walls of carbon nanotubes are fixed, and Table I displays the properties of cylindrical pores and their internal molecular numbers at different pore sizes. Although carbon nanotubes are significantly different from the complex functional group structures of real organic matter such as kerogen, their all-carbon composition and smooth molecular wall surface can exclude other factors from influencing the phase state characteristics of the internal confined fluid other than pore diameter and pore geometry.<sup>61</sup> Both slit pore and cylindrical pore models employ periodic boundary conditions in the three-dimensional direction to achieve greater consistency between the

**TABLE I.** Adsorption parameters of hydrocarbon fluids on kaolinite slit-like pores and carbon nanotube cylindrical pore walls with different pore diameters.  $d_m$  is the pore diameter;  $H$  is the total adsorption thickness;  $C_a$  is the amount of adsorption per unit area;  $\rho_a$  is the average density of the adsorbed phase;  $\rho_f$  is the average density of the free phase;  $r_{am}$  and  $r_{av}$  are the mass and volume ratio of fluid adsorbed, respectively;  $A_m/V$  is the pore surface area to volume ratio.

Pore types and loading fluids	$d_m$ (nm)	$H$ (nm)	$C_a$ (mg/m <sup>2</sup> )	$\rho_a$ (g/cm <sup>3</sup> )	$\rho_f$ (g/cm <sup>3</sup> )	$r_{am}$ (%)	$r_{av}$ (%)	$A_m/V$
Kaolinite slit-like (n-octane)	0.42	0.42	0.121	0.581	...	100.00	100.00	2.398
	0.47	0.47	0.170	0.728	...	100.00	100.00	2.146
	0.50	0.50	0.194	0.776	...	100.00	100.00	2.000
	0.86	0.86	0.242	0.562	...	100.00	100.00	1.160
	0.88	0.88	0.291	0.664	...	100.00	100.00	1.142
	0.91	0.91	0.339	0.746	...	100.00	100.00	1.099
	1.11	1.11	0.388	0.699	...	100.00	100.00	0.902
	1.30	1.30	0.436	0.672	...	100.00	100.00	0.770
	1.35	1.35	0.485	0.717	...	100.00	100.00	0.740
	1.56	1.56	0.545	0.700	...	100.00	100.00	0.641
	1.81	1.81	0.606	0.671	...	100.00	100.00	0.553
	1.93	1.93	0.666	0.692	...	100.00	100.00	0.519
	2.12	2.12	0.727	0.687	...	100.00	100.00	0.473
	2.27	2.27	0.788	0.695	...	100.00	100.00	0.441
	2.36	2.36	0.848	0.720	...	100.00	100.00	0.424
	2.60	2.60	0.909	0.700	...	100.00	100.00	0.385
	2.83	2.83	0.964	0.685	...	100.00	100.00	0.353
	4.27	2.89	0.965	0.737	0.700	66.03	67.06	0.234
	5.74	2.79	0.958	0.744	0.693	48.44	48.65	0.174
	7.15	2.87	0.968	0.729	0.693	39.52	40.21	0.140
8.63	2.81	0.943	0.728	0.688	32.02	32.51	0.116	
11.50	2.90	0.966	0.681	0.687	24.67	25.23	0.087	
14.21	2.71	0.916	0.699	0.689	18.79	19.09	0.070	
Carbon nanotube cylindrical (n-hexane)	1.64	0.77	0.242	0.627	...	100.00	100.00	2.591
	1.74	0.87	0.380	0.873	...	100.00	100.00	2.299
	2.70	1.35	0.550	0.814	...	100.00	100.00	1.480
	3.65	1.83	0.723	0.792	...	100.00	100.00	1.095
	4.60	2.30	0.898	0.781	...	100.00	100.00	0.870
	5.72	2.86	1.039	0.727	...	100.00	100.00	0.699
	6.66	3.33	1.211	0.727	...	99.68	99.99	0.601
	7.75	2.86	1.232	0.683	0.980	90.35	93.07	0.516
	8.74	2.28	1.200	0.704	0.689	78.40	78.04	0.458
	9.80	2.30	1.205	0.685	0.696	68.47	71.86	0.408
	11.88	2.40	1.246	0.686	0.654	62.24	61.12	0.337
	13.94	2.25	1.276	0.659	0.675	54.95	55.57	0.287
	Graphene-slit-like (n-hexane)	10.05	3.53	1.218	0.691	0.635	36.08	35.09

microscopic simulation results and the macroscopic thermodynamic properties. Despite the fact that petroleum is a complex mixture of saturated hydrocarbons, aromatic hydrocarbons, resins, and asphaltenes, only n-alkanes were used in this study to represent confined hydrocarbon fluids within shale pores in order to exclude the effects of other factors [Fig. 2(c)], as previous research has demonstrated that the most abundant component of crude oil is saturated hydrocarbons.<sup>50,62</sup>

N-octane and n-hexane were chosen to study the phase state characteristics of fluids confined in slit pores and cylindrical pores, respectively.

In addition, because alkanes with six or more carbons are regarded as entirely flexible, all alkanes within the pores retain their flexibility.<sup>63</sup>

Figure 2(c) depicts the initial molecular models of slit and cylindrical pores and alkanes with varying pore diameters created in this study.

### C. Simulation details and models

The MD simulations in this paper were all conducted using the open-source molecular simulation software GROMACS 2018.8.<sup>64,65</sup>

All simulations were performed using real-space particle mesh Ewald (PME) electrostatics, with the van der Waals cutoff radius set to 1.2 nm based on the original force field parameters used for simulations in this work.<sup>66</sup> Each simulation was initiated using the energy minimization algorithm of the steepest descent method, and convergence was attained when the highest force on every atom in the system was less than  $100 \text{ kJ mol}^{-1} \text{ nm}^{-1}$ . For slit-like pores, we performed MD simulations in the NPT ensemble ( $T = 298 \text{ K}$ ,  $P = 0.1 \text{ MPa}$ ) with a 10 ns equilibration period with 0.1 ps time step. By lowering the energy state of the system, the equilibrium molecular configuration in the energy stable state was reached, and the macroscopic thermodynamic characteristics of the system were statistically assessed utilizing the 5 ns molecular trajectories of the system after equilibrium. For the cylindrical pores, we performed MD simulations using the NVT ensemble at a constant temperature of 298 K for the same duration as for the slit pores. After system equilibration was reached, the final 5 ns molecular trajectory file was also utilized for data analysis. During the simulation, the system's temperature and pressure were regulated by the Nosé–Hoover thermostat and the Parrinello–Rahman barostat, respectively.<sup>37</sup> Notably, in this simulation, the nanotube matrix walls are fixed to ensure a smooth and uniform surface, but this does not affect the interaction with the internal hydrocarbon fluid. Furthermore, both the clay mineral kaolinite matrix walls and the hydrocarbon fluid retain their flexible properties. The convergence of the simulation system determines the credibility and accuracy of the simulation outcomes. Therefore, this study introduced the DynDen method to consider changes in the spatial density distribution as a criterion for assessing system convergence. The method details are shown in Sec. 3.2 of the [supplementary material](#).

The ClayFF<sup>67</sup> and CHARMM36<sup>68,69</sup> force fields were employed to simulate the clay mineral kaolinite matrix wall surface and the confined hydrocarbon molecules inside, while the CHARMM36 force field was used to simulate carbon nanotubes and their internal hydrocarbon molecules. Detailed force field parameters are collected in the [supplementary material](#) (Tables S4 and S5). Previous research on the coupling of these two force fields has demonstrated that the ClayFF and CHARMM36 force fields can accurately reproduce the interaction properties of hydrated mineral surfaces with organic molecules, whereas the CHARMM36 force field can adequately characterize carbon nanotubes and their surface properties.<sup>70</sup> Previous simulations have demonstrated that the adsorption of molecules such as acetate and ammonium to quartz surfaces assigned with CHARMM36 and ClayFF are comparable to with both *ab initio* molecular dynamics and experimental x-ray reflectivity data.<sup>37,40,49,71</sup> Quantity and length of hydrogen bonding between organic molecules and mineral surface matched DFT and XRF data within error. Lorentz–Berthelot mixing rules for van der Waals contacts are used in both the CHARMM36 and ClayFF force fields and have been utilized to describe the intermolecular organic matter–clay interactions.

Snapshots of molecular arrangement are generated with VMD 1.9.4 software, and the statistics of the number of molecules in distinct phase states are written in TCL and calculated using VMD.<sup>60</sup> The thermodynamic data of the simulated systems in this paper were gathered using the GROMACS 2018.8 analytical tools and calculated with MATLAB R2020b analysis. In the manuscript, the two-dimensional (2D) density distribution of the confined fluid is based on the distribution characteristics of the time-averaged molecular mass density in the

two directions after reaching equilibrium. The data were generated using MATLAB, following the export of information with the GROMACS densmap.

### III. RESULTS AND DISCUSSION

#### A. Density distribution and molecular arrangement characteristics of confined hydrocarbon fluids in pores of different geometries

By comparing the one-dimensional (1D) and two-dimensional (2D) density distributions and molecular arrangement of hydrocarbon fluids in pores with varied sizes and geometries, we have analyzed the characteristics of nano-confined hydrocarbon fluids. [Figure 3](#) depicts the 1D and 2D density distributions and molecular arrangement of hydrocarbon fluids in slit-like pores with varying pore diameters. Whereas the 1D density distribution of the fluid [[Fig. 3\(a\)](#)] is a continuous mass density distribution of fluid molecules at 0.03 nm intervals along the Z-direction of the vertical pore wall in accordance with Eq. (S3) in the [supplementary material](#), the spatial distribution properties of the molecules within pores [[Fig. 3\(b\)](#)] provide a snapshot of the equilibrated system. [Figure 3\(c\)](#) depicts the 2D density distribution corresponding to the final frame snapshot of the molecule in [Fig. 3\(b\)](#).

As shown in the 1D density distribution in [Fig. 3\(a\)](#), the interaction of the kaolinite with the internal hydrocarbon fluid produces a significant oscillatory pattern in the mass density near the wall surface, and this trend increases with decreasing pore diameter. At small pore diameters ( $d_m < 4 \text{ nm}$ ), the intermolecular affinity between the mineral and the fluid causes the internal space to be fully occupied by adsorbed phase fluids, with no regions of free state fluids present. When the pore diameter increases and bulk phase fluid appears in the internal space, the bulk phase fluid mass density remains unchanged. The mean value of  $0.6914 \text{ g/cm}^3$  for the bulk phase fluid density of slit-like pores based on Eq. (S6) (in the [supplementary material](#)) was independently calculated for the pore size range 4.266–14.211 nm, which is in good agreement with the results independently predicted using the National Institute of Standards and Technology (NIST) Chemistry Webbook ( $0.6986 \text{ g/cm}^3$ ),<sup>72</sup> demonstrating the validity and accuracy of the results of this simulation. Additionally, we discovered that the peak adsorption density and the number of adsorbed layers decreased with increasing pore size and stayed constant after the pore diameter reached approximately 4 nm, which is consistent with earlier studies.<sup>41</sup> Due to the complex composition of shale material and crude oil, the interaction between different pore walls and different confined fluids is significantly different. Furthermore, variations in formation temperature and pressure can lead to deviations in fluid–wall interactions, so the lower limit of adsorption in slit pores can be affected by a number of factors and vary slightly. The purpose of this study is to isolate the effect of pore size and pore geometry on the internal restricted fluid phase states; consequently, the previously listed factors will not be discussed.

On the basis of the 2D density distribution of the confined fluid in [Fig. 3\(c\)](#), the peak mass interval caused by the formation of an adsorption layer on the solid wall can be identified. Due to fluid–wall interactions, the fluid molecules form a regular “solid-like” adsorption layer close to the pore wall. The fluid molecules within the adsorption layer have a low energy steady-state characteristic distribution, and their molecular diffusion capacity is low in comparison to the bulk phase fluid.<sup>50</sup> Moreover, as the pore diameter grows, the number of

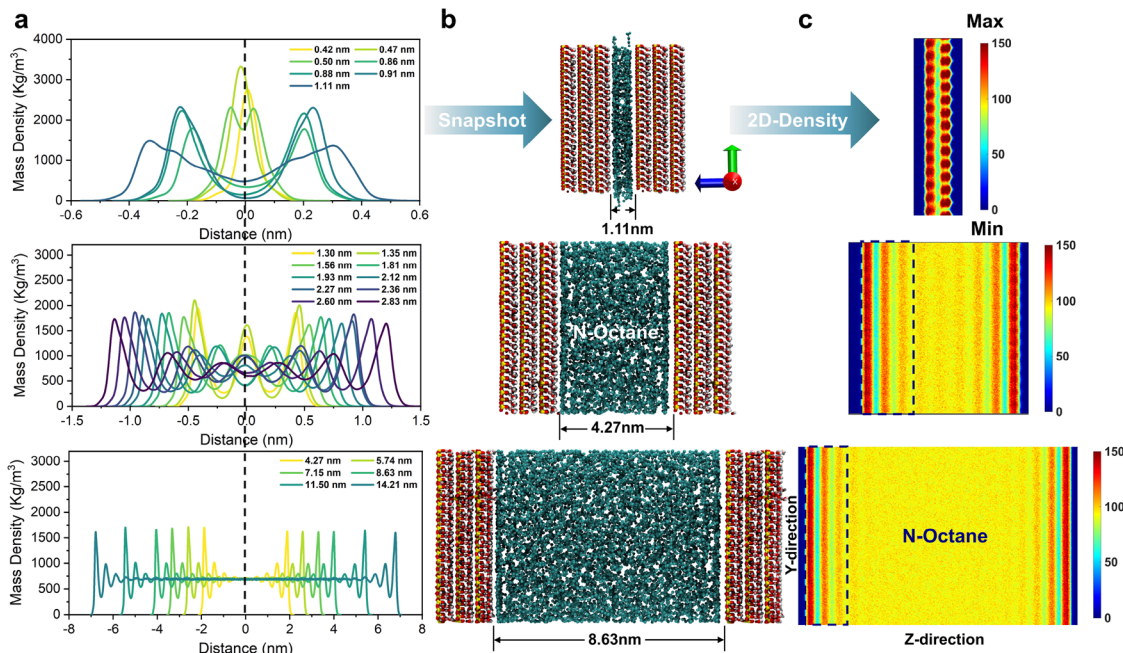


**FIG. 3.** 1D and 2D density distributions of octane in kaolinite slit-like pores of different pore sizes and molecular arrangement characteristics within the pores. (a) 1D mass density distribution of octane in different pore sizes, the legend indicates the pore size associated with the fluid density curves; (b) snapshot of the equilibrium molecular configuration of octane, where cyan represents the carbon atoms of n-octane, with hydrogen atoms omitted to more clearly visualize the distribution characteristics of octane near the clay surfaces; and (c) 2D density in y–z-direction distribution of octane corresponding to the snapshots of molecular configurations.

adsorption layers of the fluid contained internally rises in a stepwise fashion. This indicates that the number of adsorption layers grows from one layer to two layers when the pore size is less than 1.11 nm [top of Fig. 3(c)] and from two layers to six layers (i.e., three adsorption layers on one wall) when the pore size is around 4 nm. As the pore size continues to rise, the bulk phase fluid is generated, resulting in a constant number of six adsorption layers on the pore wall. Consequently, based on the preceding analysis, we hypothesize that the adsorption layer of the confined fluid in the nanopore will form layer by layer as the system reaches low energy steady-state and that the interaction between the molecules of the adsorption layer and the wall surface will gradually decrease as the distance to the center of the pore increases. Due to the superposition effect of the contact between the walls and the fluid on both sides, all fluid molecules are adsorbed into the pore space when the pore size is tiny. The two-dimensional density distribution of fluid molecules in the 1.11 nm pore diameter, as depicted in Fig. 3(c), demonstrates that the superposition of fluid–wall interactions results in a regular arrangement of fluid molecules, which is also related to the lattice symmetry of the mineral walls.

Figure 4 illustrates the 1D and 2D density distributions and molecular configuration features of hydrocarbon fluids within cylindrical pores of various pore sizes. The 1D density distribution of the fluid [Fig. 4(a)] is the continuous mass density distribution of fluid molecules along the X-direction of the vertical cylindrical pore wall calculated using Eq. (S3) (in the supplementary material). As with the fluid in the slit pore, there is a clear oscillatory feature in the density of the fluid close to the wall. Unlike slit-like pores, the 1D density distribution along the x-axis solely reveals the oscillatory characteristics of the fluid in the cylindrical pore near the wall [Fig. 4(a)]. However, due to the

time-averaged molecular density being statistically assessed in a single direction within a 3D box, a higher density is observed in the central region of the pore compared to its proximity to the wall. Calculating the 2D density distribution of the fluid inside the cylindrical pore [Fig. 4(b)] reveals that the fluid forms a circle-like adsorption layer near the walls and expands inward in a multilayered pattern. The equilibrium configuration of the molecules also demonstrates that the hydrocarbon molecules are aligned parallel to the pore walls, forming a solid-like adsorption layer comparable to that within the slit-like pores (Fig. 4). Since Eq. (S6) (in the supplementary material) is based on the proposed 1D slit pore model, it cannot be used to calculate the average density of fluids within cylindrical pores. Based upon the simulations using post-equilibration molecular trajectory data, this study calculates the average number of molecules in distinct phase states after equilibrium. By counting the number of free molecules in the pore size range of 7.75–13.94 nm, the mean bulk phase fluid density was calculated to be  $0.6672 \text{ g/cm}^3$ , which is also in good agreement with the results of the NIST Chemistry Webbook ( $0.6606 \text{ g/cm}^3$ ), demonstrating the accuracy of the cylindrical pore simulation results.<sup>73</sup> Moreover, to compare the difference in the phase state of the fluid in the slit pore under the same wall conditions, the phase state characteristics of the fluid in the slit pore under the same graphene wall conditions were simulated in this research [Fig. 4(a), slit pore]. It is noteworthy that we compared the differences in the impact of graphene and kaolinite slit pores on the behavior of saturated hydrocarbon fluids, showing that the wall material has a relatively minor effect on the adsorption characteristics of internal hydrocarbon molecules. For detailed comparisons, see Sec. 5 in the supplementary material.

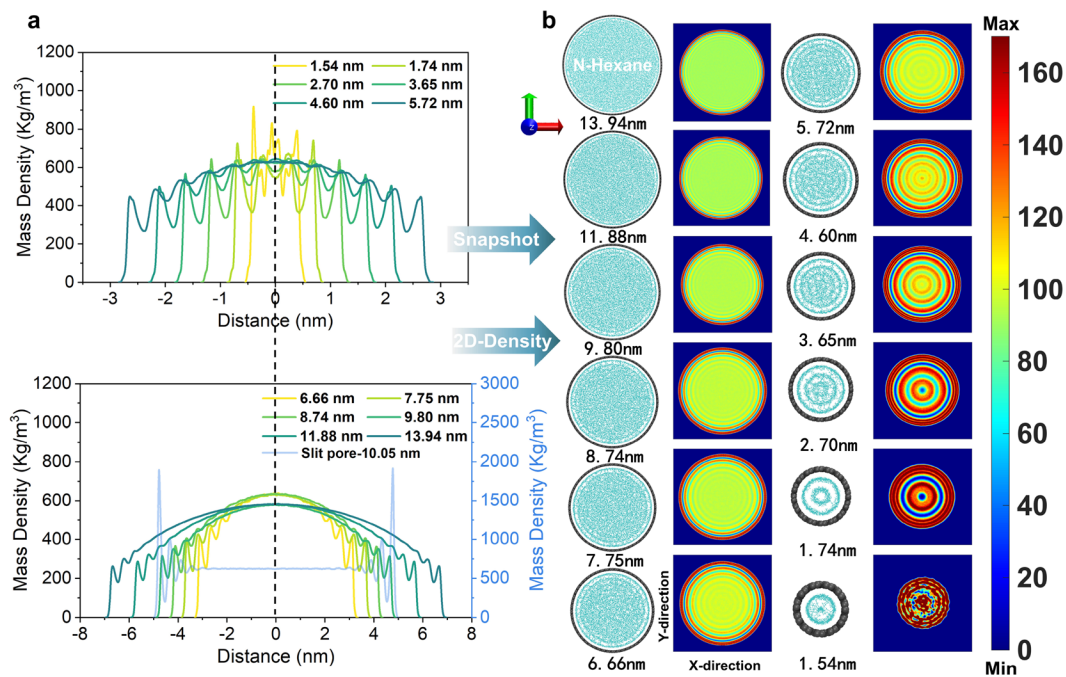


**FIG. 4.** 1D and 2D density distributions and molecular arrangement characteristics of hexane within carbon nanotube cylindrical pores of different pore diameters. (a) 1D mass density distribution of hexane in the X-direction of the box, the legend indicates the pore size associated with the fluid density curves; (b) snapshots of equilibrium molecular configurations (cyan for n-hexane) of hydrocarbon fluids in different pore diameters and the corresponding 2D density in XY-direction distribution of fluids.

The 2D density distribution of the fluid demonstrates that the fluid's behavior in the cylindrical pore differs significantly from that in the slit-like pore [Fig. 4(b)]. When the pore diameter is smaller than 7 nm, the number of adsorption layers grows as pore size increases, reaching a maximum of 7 nm and a total of seven layers. The number of adsorbed layers reduces with the appearance of free state fluid when the pore size is greater than 7 nm, but it remains constant at five layers after the pore size reaches 9 nm. Moreover, for cylindrical pores, the fluid is completely adsorbed when the pore size reaches approximately 7 nm, which is nearly double that of slit pores. This implies that with cylindrical pores, the fluid has a greater interaction with the solid walls than it does with slit pores and that the influence of the pore wall geometry is not negligible. In Sec. III D, we will discuss the mechanics underlying this phenomenon.

## B. Phase state characteristics of confined hydrocarbon fluids in pores of different geometries

The fluid phase state characteristics for various equilibrium configurations of the system were computed by extracting the mass density distribution of confined fluids in slit pores and cylindrical pores of varying pore sizes, as shown in Table I. Comparing the adsorption capacity per unit area ( $C_{ad}$ ) of confined fluid in various pore geometries and pore sizes (green dotted line in Fig. 5) reveals that the  $C_{ad}$  of confined fluid in slit-like pores tends to grow and then remain constant as the pore size increases. When the pore size is smaller than 2.8 nm, the  $C_{ad}$  of the mineral wall surface grows rapidly to 0.96 mg/m<sup>2</sup>, while the hydrocarbon fluids are completely distributed in the interior of

the pores in a laminar adsorption state, with the adsorption layer increasing from 1 to 6 layers gradually [Fig. 5(a), bottom right].  $C_{ad}$  of the mineral pore wall to the internal fluid is essentially constant, averaging 0.953 mg/m<sup>2</sup>, as the pore size increases above 2.8 nm. This implies that the interaction of clay mineral walls with hydrocarbon fluids in this study is concentrated around 1.4 nm from the wall's surface, whereas the minimum adsorption pore diameter for mineral slit pores is 2.8 nm.

As seen in the red dotted line in Fig. 5(a), the  $C_{ad}$  of the cylindrical pore wall for the fluid contained within the pore tends to increase rapidly at pore diameters less than 7 nm, with a swift rise from 0.242 to 1.211 mg/m<sup>2</sup>. Once the pore size is more than 7 nm, the amount of hydrocarbon fluid adsorbed per unit area of the wall tends to increase slowly as the pore size increases, reaching roughly 1.276 mg/m<sup>2</sup> when the pore diameter approaches 14 nm. Consequently, the wall surface interaction with confined fluids can extend to a maximum of 3.5 nm near the wall surface for cylindrical pores, while the lower limit adsorption pore diameter can approach 7 nm. Since the specific surface area of cylindrical pores of the same length increases as pore size increases, resulting in more adsorption sites on the walls, their hydrocarbon adsorption capacity per unit area does not remain constant but gradually increases after reaching the lower limit of adsorption.

The thickness of the fluid adsorbed on the pore wall is a crucial parameter for quantitatively describing the phase states of the fluid at the nanoscale and is required by a variety of quantitative characterization methods, including theoretical and volumetric methods, in order to introduce an interaction parameter for the pore wall with the fluid. As shown in Fig. 5(b) and Table I, the fluctuation of adsorption thickness (H) within slit-like and cylindrical pores with varied pore

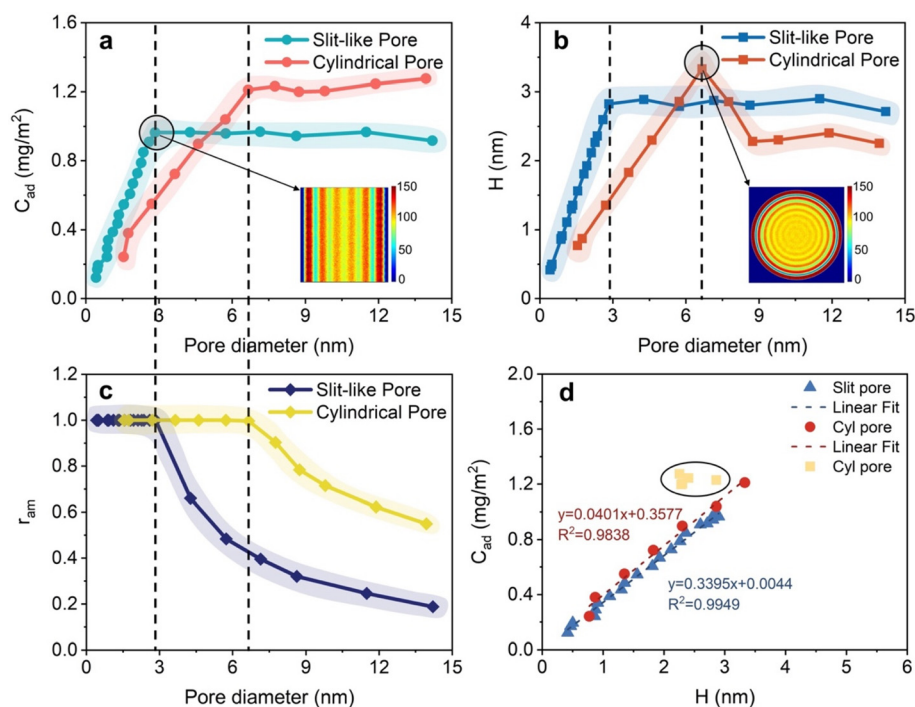


**FIG. 5.** Analysis of the fluid behavior inside slit pores (octane) and cylindrical pores (hexane) with different pore diameters. (a) Variation of  $C_{ad}$  of the fluid on the walls with pore diameter; (b) variation of the adsorption thickness of the fluid on the walls with pore diameter; (c) variation of the adsorption mass fraction of the fluid on the walls with pore diameter; and (d) relationship between  $C_{ad}$  and adsorption thickness of the fluid for different pore diameters, where red dots and yellow squares represent cylindrical pore data. Red dots correspond to pore diameters smaller than the lower limit of adsorption, while yellow squares represent pore diameters greater than this limit.

diameters was separately estimated in this study. For slit pores, it can be observed that the  $H$  of the wall surface to the internal fluid follows the same pattern as the  $C_{ad}$  [Fig. 5(b), blue dotted line]. When the pore size was increased up to 2.83 nm,  $H$  rose from 0.42 to 2.83 nm. The adsorption thickness remained constant as the pore size increased, and the average adsorption thickness after the pore size exceeded the lower limit of adsorption was 2.83 nm. For cylindrical pores, the adsorption thickness of the wall increases with increasing pore size for pore diameters less than 7 nm [red dashed line in Fig. 5(b)], and the number of adsorption layers progressively increases from two to seven layers. When the pore size approaches 7 nm, the fluid inside the pore occurs in a circle-like adsorption pattern [lower right corner of Fig. 5(b)] with an adsorption thickness of 3.35 nm. As the pore diameter of the cylindrical pores continued to rise, free hydrocarbons were gradually present within the center of the cylindrical pores, resulting in a reduction of the adsorption layer from seven to five layers. Therefore, the wall thickness of the adsorbed fluid decreases once the pore diameter exceeds 7 nm and remains constant after the pore diameter reaches roughly 9 nm, with an average adsorption thickness of 2.31 nm.

Analyzing the relationship between  $H$  and  $C_{ad}$  for different pore sizes in slit-like pores revealed a clear linear correlation [Fig. 5(d)], indicating that the wall  $C_{ad}$  parameters proposed in this paper have the same implications as the wall adsorbed fluid thickness both can reflect the interaction strength of the wall surface to the pore-confined fluid at the microscopic scale. As depicted by the red dots in Fig. 5(d),  $C_{ad}$  exhibits a linear relationship with  $H$  when the pore size is smaller than the lower limit of adsorption for cylindrical pores. Nonetheless, as the pore size of the cylindrical pore increases, the correlation between  $C_{ad}$  and  $H$  diminishes. This occurs because the adsorption thickness of the cylindrical pore slightly decreases and then stabilizes when the

pore size exceeds the lower limit of adsorption, and the adsorption capacity of its pore wall for the fluid experiences minor alterations.

To quantitatively characterize the phase state characteristics of hydrocarbon fluids in slit pores and cylindrical pores of various pore sizes, molecular trajectory files of the equilibrium MD simulation system were obtained, and the number of molecules occurring in the adsorbed and free states was separately calculated. To quantify the adsorbed mass ratio of the confined fluid within the different pore diameters, the ratio of adsorbed molecules to the total number of hydrocarbon molecules in the system was calculated, and the results are displayed in Fig. 5(c) and Table I. Once the pore size approaches the lower limit of adsorption, the relative fraction of fluid mass adsorbed within the two pore geometries falls exponentially with increasing pore size. For the same pore diameter, the amount of fluid adsorbed in cylindrical pores was substantially more than in slit-like pores. Table I presents the fluid behavior parameters of hydrocarbon fluids in the slit pores of 10.05 nm-diameter graphene. A comparison with the slit pores of the mineral walls reveals that the interaction of hydrocarbon fluids within the graphene walls is marginally greater than that of the clay mineral walls, and that the  $C_{ad}$  and  $H$  of the graphene walls were approximately 1.2 times greater than those of the mineral walls. However, the lower limit pore diameter for adsorption varied by a factor of around 2.5 depending on pore shape. This suggests that, at the nanoscale, the influence of pore geometry on the phase state of the fluid within the pore is far greater than the influence of the interaction between the various pore walls on the fluid.

### C. Estimation methods validation and quantitative evaluation of nano-confined fluid phase states

A quantitative evaluation model was established to characterize the phase state characteristics of fluids confined within nanoscale

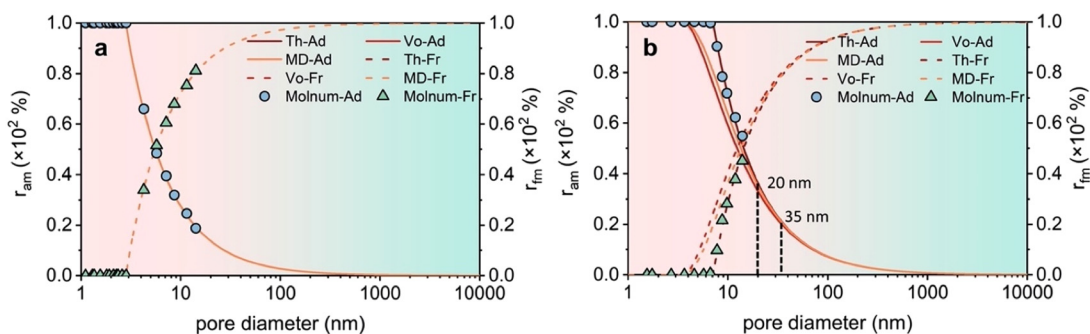


**FIG. 6.** Variation of the mass ratios of fluids in the adsorbed and free states in slit and cylindrical pores with logarithmic pore diameter. (a) Variation of the octane's mass ratio in the slit pore with pore diameter; (b) variation of the hexane's mass ratio in the cylindrical pore with pore diameter. Th-Ad, Vo-Ad, and MD-Ad represent the mass ratios of adsorbed fluids based on theoretical, volumetric, and model methods, respectively; Th-Fr, Vo-Fr, and MD-Fr represent the mass ratios of free fluids based on the three methods; Molnum-Ad and Molnum-Fr represent the mass ratios of adsorbed and free hydrocarbon molecules based on MD simulation trajectory files.

pores. The adsorbed and free state mass ratios estimated from MD simulations of fluids in slit and cylindrical pore systems were compared with the results calculated by Eq. (10), and the results of both computations are depicted in Fig. 6. Notably, in order to ensure consistency between the fluid behavior parameters calculated from MD simulations based on different pore walls and the model, the parameters corresponding to slit-like pores were derived from the simulation results of mineral pores with a pore diameter of 8.63 nm. In addition, the parameters corresponding to cylindrical pores were derived from simulation results of slit-like pores on graphene walls with a pore size of 10.05 nm and calculated using the version of cylindrical pores according to Eq. (10). To evaluate the accuracy and applicability of the results of various models, the volumetric and theoretical method results were calculated using Eqs. (S7)–(S10) (in the [supplementary material](#)) with identical fluid behavior parameters, respectively.

As illustrated by the complete overlap of the distribution curves of the adsorbed and free fluid mass ratios against pore diameter calculated by the three methods, shown in Fig. 6(a), the model proposed here is in complete agreement with the volumetric and theoretical methods for the evaluation of the phase states of nano-confined fluids. In addition, the results for the mass ratio of adsorbed and free fluid based on the trajectory file after equilibration of the MD simulation system are in strong agreement with the evaluation results of the three methods [Fig. 6(a), spherical and triangular points], confirming that all three methods accurately characterize the phase states of the fluid within the slit-like pores at different pore diameters. In the case of cylindrical pores, the evaluation of fluid phase states using the three models is influenced by the variance in pore geometry [Fig. 6(b)]. Due to the utility of molecular simulations in describing microscopic thermodynamic changes,<sup>36</sup> the mass ratios of adsorbed and free fluid based on the trajectory file of the equilibrated system are deemed accurate here. Comparing the results of the MD simulation with those of the model calculation reveals that the theoretical method agreed better with the simulation results, indicating that it was more applicable than the volumetric method and the model method for characterizing the confined fluid behavior within the cylindrical pore space. As observed from the derivation of Eqs. (S8) and (S10) (in the [supplementary material](#)), the lower limit of the adsorption pore diameter for both the volumetric and model methods is twice the thickness of the fluid adsorbed at the wall when all the fluid in the pore is adsorbed, i.e.,  $2H$ .

Since simulation results for slit pores are used for the fluid behavior parameters, the lower limit of the adsorption pore diameter obtained by these two methods is unaffected by the pore geometry. For the theoretical method, on the other hand, the lower limit of the adsorption pore size is  $\tau H$ , and the thickness of the fluid adsorbed corresponding to the different geometry of the walls is corrected by introducing a pore shape factor  $\tau$ , so that its calculation results match better with those of the MD simulation. Comparing the deviations of the distribution curves of the fluid phase states calculated by the three methods reveals that the model proposed in this paper begins to deviate from the theoretical method when the pore size is less than 20 nm, indicating that the proportion of fluid adsorption calculated by the model is small for the same pore diameter in this pore range. The volumetric method deviates from 35 nm and achieves the lowest adsorption ratios for fluids contained within the cylindrical pores. On the basis of the preceding analysis, it is possible to conclude that the fluid behavior parameters obtained from the MD simulations in conjunction with the quantitative evaluation model proposed in this study can adequately characterize the fluid phase states in slit pores with different pore diameters. In the case of cylindrical pores, the results of the MD simulation can be substituted into the theoretical method [Eq. (S10) in the [supplementary material](#)] to estimate the fluid phase states features of confined fluids.

Based on the validated model and molecular dynamics simulation results for slit-like pore systems in clay (kaolinite) minerals, we characterized the fluid phase state distribution as a function of pore diameter across different pore geometries (Fig. 7). It should be noted that this calculation employs MD-simulated data of octane within kaolinite slit-like pores, which is influenced by various factors such as pore wall composition, fluid fraction, and external environment (temperature and pressure). These factors are not discussed in this paper, as they are not relevant to the subject matter of this paper. As indicated by the model calculations, as the pore size increased, the proportion of adsorbed fluids reduced rapidly, while free state fluids emerge and occupy the bulk of the pore space (Fig. 7). When the pore size was lowered to a diameter comparable to the adsorption thickness, the mass ratio of the fluid adsorbed within the pore space reached 1. At this moment, all fluids confined within a pore are in an adsorbed state, and the fluid mobility is negligible. Therefore, the pore size of the slit pores can be regarded as the lower limit of adsorption, which corresponds to

2.8 nm of the lower limit of hydrocarbon fluid adsorption inside the pores of kaolinite used in this study, which is consistent with the parameters calculated by Li *et al.* based on the experimentally obtained data.<sup>35</sup> The lower limits of adsorption for alkane fluids in cylindrical and spherical pores are 5.6 and 8.4 nm, respectively. Previous studies indicate that the minimum throat (which may be viewed as a cylindrical pore) pore size for shale that permits shale oil penetration is approximately 20 nm.<sup>9</sup> There is a discrepancy with the lower limit of adsorption for cylindrical pores calculated in this study, but it should be noted that this parameter is a theoretical conclusion for the adsorption of a single alkane fluid on a smooth wall at the molecular scale. The transition from slit to spherical wall geometry increases the lower limit of adsorption pore size significantly, indicating that the complexity of the pore structure increases this threshold, which is also influenced by a number of other variables, such as formation temperature and pressure conditions, fluid composition, and pore wall properties.

Based on the quantitative evaluation of the phase states of fluids within pores of various geometries and compositions, we classified the fluids confined by solid walls into three regions, as depicted in Fig. 7. The region closest to the solid wall is designated as the fully adsorbed region ( $d_m > 8.4$  nm), where it is expected that the fluid interacts most strongly with the solid wall and associated strongly bound layers of organic molecules and is distributed in an adsorbed state in the pore space with almost negligible mobility. As the pore size increases, the interaction between the fluid at the center of the pore and the pore wall weakens and the fluid in its free state gradually emerges. This region is distinguished as the pore wall's strong influence region ( $8.4 \text{ nm} < d_m \leq 85$  nm). Since the mass ratio of the adsorbed fluid to flowing fluid in this region is larger than 10%, the adsorbed fluid fraction cannot be neglected, and the flow capacity of the fluid confined in the pore grows rapidly with increasing pore diameter. As the pore size continues to expand, the mass ratio of the wall-to-fluid interaction fraction falls below 10%, and we define this region as the pore wall's weak influence region ( $d_m > 85$  nm). At this time, the influence of flow-wall interactions on the internal fluid behavior can be disregarded as the fluid is predominantly in the free state. Comparing the

results of the theoretical and modeling methods based on the same parameters [Figs. 7(a) and 7(b)], we discovered that the model proposed in this paper only deviates from the lower limit of adsorption influenced by the pore geometry but is in complete agreement with the theoretical method in determining the range of the wall strength influence zone. Consequently, both methods permit a quantitative evaluation of the phase states of fluids within nanopores.

## D. Mechanism of the effect of pore diameter and pore geometry on nano-confined fluid phase state

To elucidate the mechanism by which various pore geometries and pore diameters contribute to the nano-confined fluid, the diffusion coefficient of the fluid and the interaction energy of the solid wall surface with the fluid were separately estimated using MD simulations (Table II). Figures 8(a) and 8(b) show the estimated diffusion coefficients for hydrocarbon fluids in kaolinite slit-like pores and carbon nanotube cylindrical pores, respectively. It can be observed that the diffusion coefficients of the fluids within both pore shapes increase linearly with increasing pore diameter, indicating that the flow capacity of the fluids increases with increasing pore diameter. This result supports the quantitative evaluation of the confined fluid phase state characteristics in Sec. III C. Comparing the diffusion coefficients of fluids between the two pore geometries reveals that the diffusion coefficient of fluids within slit pores was not zero even when the pore size is decreased to a very small aperture (Table II). As shown in Fig. 8(a), once the pore size approached 2.8 nm, the diffusion coefficient of the fully adsorbed fluid molecules fluctuated in the range  $0.002 \times 10^{-9}$ – $1.165 \times 10^{-9}$  m<sup>2</sup>/s, showing that the fluid molecules within the slit pore continue to move in a small range while being in an adsorbed state. The diffusion coefficient of the fluid within the cylindrical pore fell to  $0.016 \times 10^{-9}$  m<sup>2</sup>/s when the pore diameter reached 1.74 nm (Table II), and the linear fitting equation enables us to determine that the internal fluid diffusion coefficient was zero when the pore diameter reached 0.37 nm [Fig. 8(b)]. As the pore walls of cylindrical pores interact substantially more with the internal fluids than those of slit pores, the diffusion coefficient of the confined fluids within

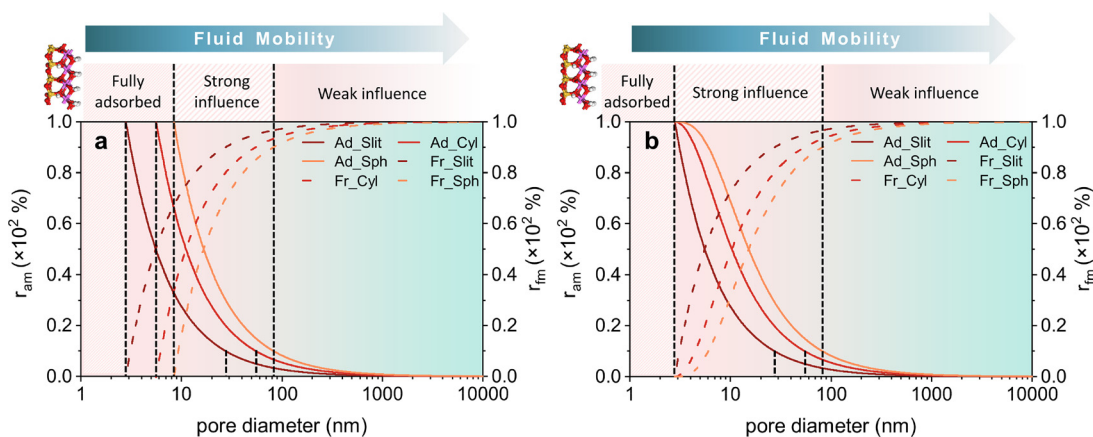


**FIG. 7.** The phase states of fluid (octane) vary with the logarithm of the pore diameter in kaolinite pores of three distinct pore shapes. (a) Variation of fluid phase state characteristics with pore diameter according to the theoretical approach; (b) variation of fluid phase state characteristics with pore diameter according to the model. Ad\_Slit, Ad\_Cyl, and Ad\_Sph represent the ratio of adsorbed mass in the slit, cylindrical and spherical pores, respectively, and Fr\_Slit, Fr\_Cyl, and Fr\_Sph represent the ratio of free mass in the three shapes, respectively.

cylindrical pores is lower than that of slit pores. The comparison of hydrocarbon fluid parameters in clay mineral and graphene slit pores obtained from MD simulations (Table I) reveals that the effect of wall composition on internal fluid phase states is relatively minor compared to the influence of wall geometry. Therefore, it can be predicted that the complexity of the pore geometry drastically limits the degree of internal fluid mobility, and for shales, the slit pores of clay minerals have a greater degree of fluid mobility than the organic pores of the cylindrical throat and ink bottle type pore.

Intermolecular interaction forces are the primary cause of non-ideal gas behavior, solution phenomena, and phase transition activities,

the calculation method of interaction energy is shown in Sec. II A 5. There are numerous forms of intermolecular interactions for the non-polar molecular system utilized in this study, though van der Waals interactions dominate, with a limited degree of electrostatic interactions due to the relatively low electric charge on the surface of the kaolinite (Table II). The interaction energy of the pore wall surface for the internal fluid has been determined here by MD simulations for different geometries and pore sizes, and its fluctuation with pore diameter is depicted in Figs. 8(c) and 8(d). As seen in Fig. 8, as the pore size decreased, the interaction energy between the wall and the internal fluid increased, which explains the progressive transition of the

**TABLE II.** Diffusion coefficients and interaction energy parameters of hydrocarbon fluids in pores of different pore diameters and geometries.  $d_m$  is the pore diameter;  $D$  is self-diffusion coefficient;  $E_{Coul}$  and  $E_{VDW}$  represent the long-range intermolecular Coulomb and van der Waals interaction terms, respectively. Values in brackets give the standard error as obtained by evaluating outcomes of parallel simulations for different hydrocarbon components.

Pore types and loading fluids	$d_m$ (nm)	$D$ ( $10^{-9}$ m <sup>2</sup> /s)	$E_{Coul}$ (kcal/mol)	$E_{VDW}$ (kcal/mol)	$E_{non-bonded}$ (kcal/mol)
Kaolinite slit-like (n-octane)	0.42	0.581	-9.77 ( $\pm 0.82$ )	-68.67 ( $\pm 0.81$ )	-78.44 ( $\pm 1.12$ )
	0.47	0.003	-8.90 ( $\pm 0.50$ )	-66.21 ( $\pm 0.55$ )	-75.11 ( $\pm 1.05$ )
	0.50	0.002	-7.60 ( $\pm 0.38$ )	-60.54 ( $\pm 0.45$ )	-68.14 ( $\pm 0.83$ )
	0.86	1.165	-3.97 ( $\pm 0.19$ )	-33.97 ( $\pm 0.73$ )	-37.94 ( $\pm 0.92$ )
	0.88	0.639	-3.81 ( $\pm 0.29$ )	-33.98 ( $\pm 0.39$ )	-37.78 ( $\pm 0.78$ )
	0.91	0.096	-3.63 ( $\pm 0.36$ )	-33.36 ( $\pm 0.46$ )	-36.99 ( $\pm 0.82$ )
	1.11	0.053	-2.86 ( $\pm 0.40$ )	-25.96 ( $\pm 0.85$ )	-28.82 ( $\pm 1.26$ )
	1.30	0.620	-2.36 ( $\pm 0.40$ )	-21.56 ( $\pm 0.28$ )	-23.92 ( $\pm 0.79$ )
	1.35	0.402	-2.28 ( $\pm 0.45$ )	-21.27 ( $\pm 0.43$ )	-23.56 ( $\pm 0.85$ )
	1.56	0.317	-2.01 ( $\pm 0.56$ )	-18.06 ( $\pm 0.50$ )	-20.07 ( $\pm 0.91$ )
	1.81	1.011	-1.68 ( $\pm 0.21$ )	-15.59 ( $\pm 0.41$ )	-17.27 ( $\pm 0.62$ )
	1.93	0.561	-1.57 ( $\pm 0.68$ )	-14.55 ( $\pm 0.98$ )	-16.12 ( $\pm 0.97$ )
	2.12	0.806	-1.38 ( $\pm 0.46$ )	-12.68 ( $\pm 0.63$ )	-14.06 ( $\pm 1.10$ )
	2.27	0.811	-1.28 ( $\pm 0.52$ )	-11.92 ( $\pm 0.42$ )	-13.20 ( $\pm 0.95$ )
	2.36	0.399	-1.24 ( $\pm 0.80$ )	-11.74 ( $\pm 0.66$ )	-12.98 ( $\pm 1.12$ )
	2.60	0.562	-1.11 ( $\pm 0.59$ )	-10.47 ( $\pm 0.81$ )	-11.58 ( $\pm 1.35$ )
	2.83	0.911	-1.03 ( $\pm 0.21$ )	-9.53 ( $\pm 0.55$ )	-10.56 ( $\pm 0.76$ )
	4.27	1.237	-0.68 ( $\pm 0.46$ )	-6.21 ( $\pm 0.45$ )	-6.89 ( $\pm 0.92$ )
5.74	1.529	-0.50 ( $\pm 0.68$ )	-4.63 ( $\pm 0.73$ )	-5.13 ( $\pm 1.35$ )	
7.15	1.519	-0.40 ( $\pm 0.52$ )	-3.68 ( $\pm 0.39$ )	-4.08 ( $\pm 0.91$ )	
8.63	1.649	-0.34 ( $\pm 0.56$ )	-3.09 ( $\pm 0.46$ )	-3.43 ( $\pm 1.02$ )	
11.50	1.912	-0.26 ( $\pm 0.80$ )	-2.32 ( $\pm 0.85$ )	-2.57 ( $\pm 1.56$ )	
14.21	1.786	-0.20 ( $\pm 0.21$ )	-1.84 ( $\pm 0.28$ )	-2.04 ( $\pm 0.49$ )	
Carbon nanotube cylindrical (n-hexane)	1.64	0.000	...	-40.84 ( $\pm 0.81$ )	-40.84 ( $\pm 0.81$ )
	1.74	0.016	...	-37.45 ( $\pm 0.55$ )	-37.45 ( $\pm 0.55$ )
	2.70	0.129	...	-26.27 ( $\pm 0.45$ )	-26.27 ( $\pm 0.45$ )
	3.65	0.225	...	-19.46 ( $\pm 0.73$ )	-19.46 ( $\pm 0.73$ )
	4.60	0.309	...	-15.47 ( $\pm 0.39$ )	-15.47 ( $\pm 0.39$ )
	5.72	0.713	...	-12.80 ( $\pm 0.46$ )	-12.80 ( $\pm 0.46$ )
	6.66	0.800	...	-10.92 ( $\pm 0.85$ )	-10.92 ( $\pm 0.85$ )
	7.75	1.050	...	-9.57 ( $\pm 0.28$ )	-9.57 ( $\pm 0.28$ )
	8.74	1.197	...	-8.45 ( $\pm 0.43$ )	-8.45 ( $\pm 0.43$ )
	9.80	1.443	...	-7.56 ( $\pm 0.50$ )	-7.56 ( $\pm 0.50$ )
	11.88	1.886	...	-6.26 ( $\pm 0.41$ )	-6.26 ( $\pm 0.41$ )
	13.94	2.100	...	-5.37 ( $\pm 0.98$ )	-5.37 ( $\pm 0.98$ )

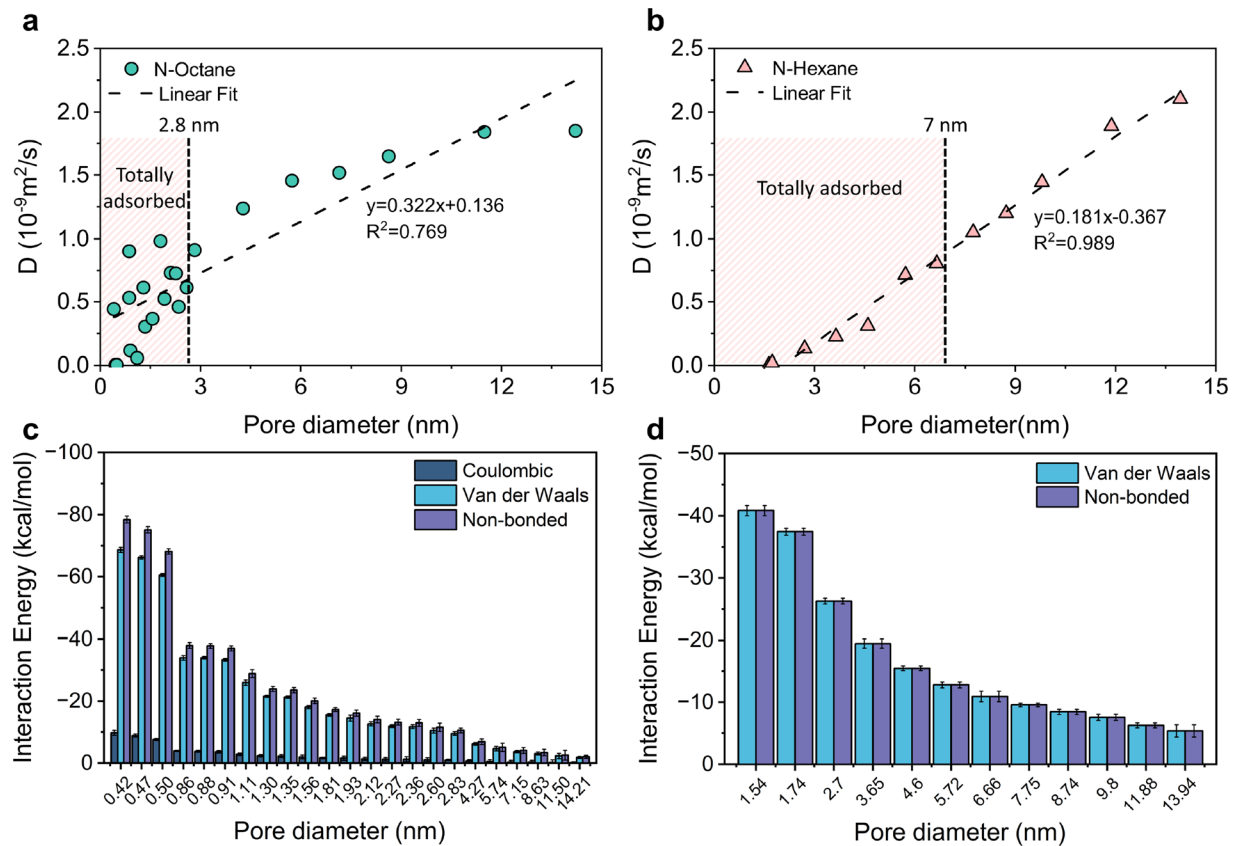


**FIG. 8.** Diffusion coefficients and wall interaction energy of fluids in pores of different geometries as a function of pore diameter. (a) Diffusion coefficients of octane in slit-like pores as a function of pore diameter; (b) diffusion coefficients of hexane in cylindrical pores as a function of pore diameter; (c) interaction energy of kaolinite slit-like pore walls on internal fluids; and (d) interaction energy of carbon nanotube cylindrical pore walls on internal fluids; where electrostatic and VDW represent electrostatic interaction energy and van der Waals interaction energy, respectively.

nano-confined fluid from a free state to an adsorbed one. For both walls, the interaction with the internal fluid is dominated by van der Waals interactions, with a small amount of electrostatic interaction between the clay mineral and the fluid due to a small charge on the wall surface [Fig. 8(c)], whereas for non-polar carbon nanotubes, the interaction with the fluid is entirely dominated by van der Waals interactions [Fig. 8(d)]. In addition, the interaction energy between the 10.05 nm graphene wall and the interior fluid was predicted to be  $-4.338 \text{ kJ/mol}$  based on the van der Waals interaction energy. The interaction energy between carbon nanotubes with a pore diameter of 9.8 nm and the internal fluid was found to be 1.8 times greater for cylindrical pores than for slit-like pores, which is similar with the results of Wang *et al.* and thus verifies Sec. III C findings.<sup>41</sup>

Figure 9(a) depicts the characteristics of the phase state distribution of nano-confined fluids derived from MD simulation results based on fluid molecules within pore systems with varying pore diameters and geometries. When the pore size of slit-like pores is smaller than the lower limit of adsorption, the fluid is arranged in layers of adsorption states within the pore space. When the pore size is less than the lower limit of adsorption, the adsorption layer is formed incrementally as the pore size increases, the pore wall adsorption site is filled with

fluid molecules prior to the formation of the second layer, and so on until the pore size reaches the lower limit of adsorption, at which point the number of adsorption layers ceases to increase and remains constant. Moreover, the pore wall generates a solid-like adsorption layer that mimics an extension of the wall, resulting in multilayer adsorption within the fluid. When the pore diameter of the cylindrical pore was less than the lower limit of adsorption, the fluid molecules were distributed in a circle-like adsorption state parallel to the pore wall. The adsorption layer formed incrementally as the pore diameter increased, and the number of layers reached its maximum when the pore diameter reached the lower limit of adsorption. In cylindrical pores, unlike slit pores, the number of adsorbed layers declined and remained constant when free fluid emerged in the center of the pore region.

By more closely studying the equilibrium configuration of fluid molecules near mineral walls, it was discovered that fluid molecules near the walls exhibited a distinct triple layer adsorption characteristic [Fig. 9(b)]. Vertical snapshots of the molecular configurations were extracted on the first and third adsorption layers and showed that the molecules in the first adsorption layer were aligned parallel to the solid wall due to the strongest interaction with the wall, and the parallel arrangement of molecules had certain preferred alignment

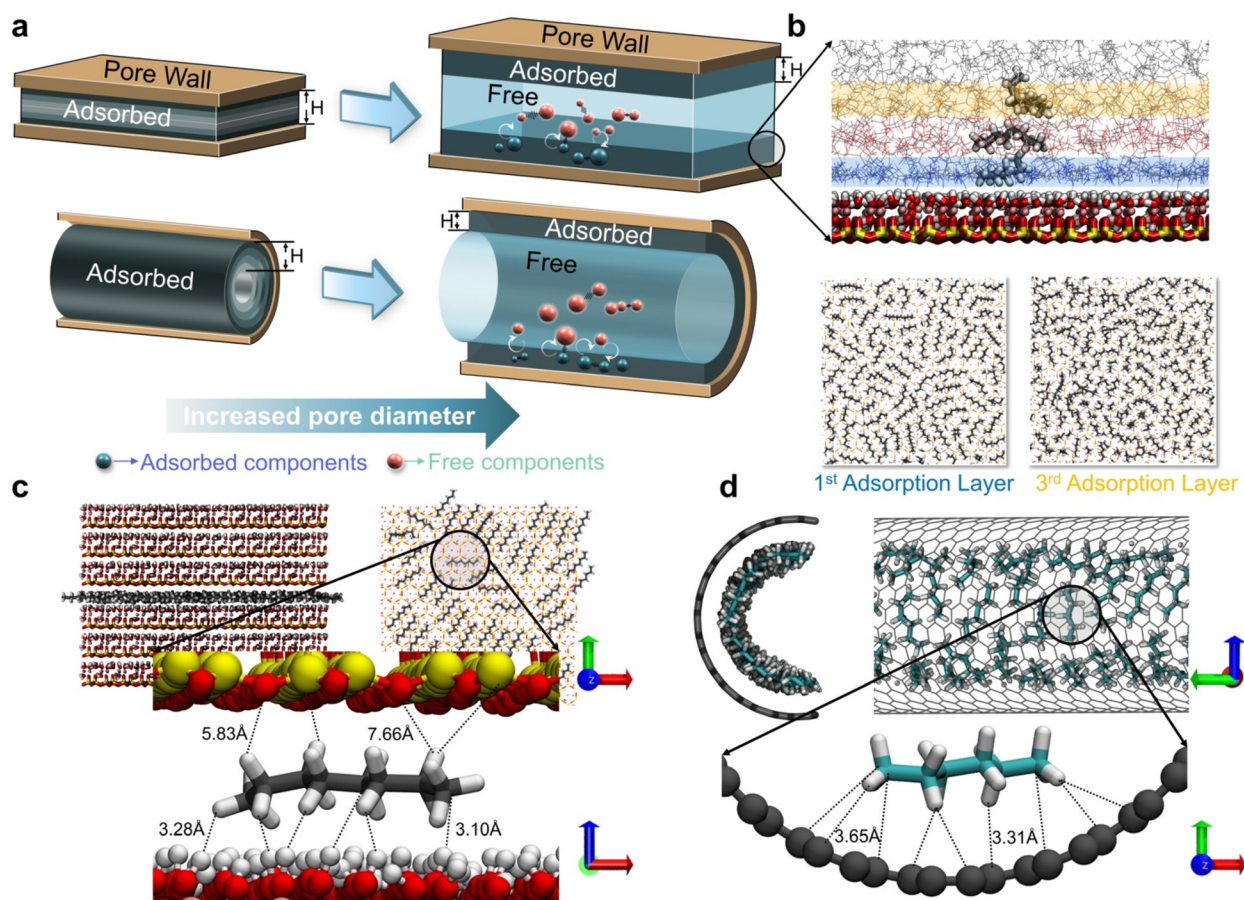


**FIG. 9.** (a) Schematic diagram of the phase state of confined fluids in different shaped pores; (b) enlarged snapshots of the molecular equilibrium configuration of different adsorption layers near the wall; (c) snapshots of the molecular equilibrium configuration of octane inside a slit-like pore of 0.42 nm; and (d) snapshots of the molecular equilibrium configuration of hexane inside a cylindrical pore of 1.74 nm.

characteristics owing to the lattice features of the underlying mineral surface lattice. In the third adsorption layer, the molecular arrangement displays a heterogeneous distribution and an abundance of molecules crossing between different adsorption layers. Even though the fluid molecules are scattered in the pore space in both the adsorbed and free states, there is still interconversion between the two states, as illustrated in Fig. 9(a). This indicates that some of the free molecules are trapped by the wall interaction and enter the adsorbed layer, however some of the adsorbed molecules are also released by the wall interaction and enter the bulk fluid phase.

In order to elucidate the microscopic mechanism of pore geometry on fluid molecule interactions, we examine the force characteristics of fluid molecules in two pore geometries [Figs. 9(c) and 9(d)]. A top view of the equilibrium configuration of the fluid molecules within the 0.42 nm pore size slit pores in the Z-direction reveals that the n-octane molecules are all distributed in the pores parallel to the walls and are predominantly oriented at  $45^\circ$ , which is associated with the hexagonal lattice characteristics of the siloxane surface of kaolinite. By measuring the distances between the atoms of one of the n-octane molecules and the two surfaces of kaolinite, it is possible to determine that the alkane

molecule is closer to the hydroxyl surface. This is because the alkane molecule is subject to both van der Waals and electrostatic interactions at the hydroxyl surface. In the pores of carbon nanotubes with a pore diameter of 1.74 nm, hexane molecules are also dispersed parallel to the walls. By measuring the distance between one of the hexane molecules and the wall, it was discovered that the alkane molecules interacted with the curved wall in multiple directions with similar forces. It may be assumed that when the interaction forces between the wall and the fluid are the same, the curved wall leads to a superposition of interactions against the same fluid molecule, hence enhancing the interaction between the wall and the fluid. Calculating the ratio of surface area to volume for slit and cylindrical pores with the same wall surface and pore diameter reveals that the ratio is four times greater for cylindrical pores than slit pores. This indicates that the specific surface area of the cylindrical pore wall is greater than that of the slit pore, resulting in higher absorption capacity.

#### IV. CONCLUSION

In this study, a method for quantitatively characterizing the phase state of nanopore-confined fluids using MD simulations is proposed,

and a quantitative evaluation model of the phase state properties of fluids is constructed and validated using MD simulations. Here, the phase state characteristics of model hydrocarbon fluids in slit-like representative mineral pores (kaolinite) and cylindrical organic pores (carbon nanotubes), both with varying pore diameters, are assessed to exemplify the method. It was determined that the lower limit adsorption pore size for kaolinite slit pores was 2.8 nm and that fluids in pores with pore sizes smaller than this were distributed in a multilayered adsorption pattern parallel to the walls. The minimum adsorption pore size for an organic cylindrical pore was found to be 7 nm. When the pore size is smaller than this, the confined fluid exhibits a radial-like adsorption state parallel to the pore wall and aligned along the cylindrical pore. The findings indicate that the adsorption amount per unit area ( $C_{ad}$ ) and the adsorption layer thickness of the slit pores grew with pore size and subsequently remained constant after the pore size exceeded the lower limit of adsorption. The  $C_{ad}$  of the cylindrical pore wall tended to increase when the pore diameter was less than the lower limit of adsorption, then increasing slowly with increasing pore diameter. When the pore size was smaller than the lower limit of adsorption, the adsorption thickness steadily increased with increasing pore diameter. As the pore size continued to expand beyond 7 nm, free fluid gradually emerged at the center of the cylindrical pores, resulting in a decrease in the adsorption thickness, which remained constant after the pore size reached approximately 9 nm.

The distribution features of fluid phase states in different shaped pores as a function of pore diameter have been estimated using fluid behavior parameters acquired from MD simulation results, and the results of three distinct quantitative evaluation methods, theoretical, volumetric, and modeling methods, were compared. For slit pores, the results of the three characterization methods exactly matched the results of molecular simulation; however, for cylindrical pores, the theoretical method resembled the molecular simulation results best for the fraction less than 20 nm. Based on the validated model, the hydrocarbon fluid's phase states in different pore shapes with varying pore sizes was characterized and it was possible to divide the nano-confined fluid into three regions: the fully adsorbed region (the pore diameter  $d_m \leq 8.4$  nm), the pore wall's strong influence region ( $8.4$  nm  $< d_m \leq 85$  nm), and the weak influence region ( $d_m > 82.5$  nm), in which the fluid becomes increasingly mobile. In the system studied, when the pore size was less than 82.5 nm, the influence of the adsorbed state component arising from fluid-wall interaction was not regarded as inconsequential.

The present study determined that the diffusion coefficient of confined hydrocarbon fluid within a cylindrical pore based on a carbon nanotube was less than that of a slit pore, and it was concluded that the complexity of the pore geometry considerably impacts the equilibrium state diffusivity of the fluid and its flow capacity. The results of the fluid-wall interaction energy calculations indicate that when the pore diameter reduced, the interaction energy of the wall surface with the internal fluid increased, with van der Waals interactions dominating the increase. The interaction energy between the cylindrical pore and the internal fluid is 1.8 times more than that of the slit-like pore. After the system had reached equilibrium, the alteration in molecular configuration demonstrated that fluid molecules distributed in the adsorbed and free states were still susceptible to interconversion. The difference in fluid adsorption capacity between cylindrical and slit pores was attributed to the superposition of forces on fluid molecules

on the curved walls and the larger specific surface area of the cylindrical pore walls. This work provides a detailed characterization of nano-confined hydrocarbon fluids in pores with varied pore shapes and pore diameters and establishes a method for quantitatively characterizing the confined fluid phase state characteristics based on MD simulations. This provides a comprehensive reference for accurate calculation of the lower limit of shale adsorption pore size and further evaluation of shale oil mobilization capability.

## SUPPLEMENTARY MATERIAL

See the [supplementary material](#) for methods for quantitatively calculating fluid spatial density based on molecular simulation results and two methods for quantitatively characterizing hydrocarbon phase characteristics; the model parameters, force field parameters, and convergence criteria of the molecular dynamics simulations conducted in this study; and discussion on the differences in the impact of two different types of wall surfaces on the behavior of internal hydrocarbon fluids mentioned in the manuscript.

## ACKNOWLEDGMENTS

We would like to express appreciation for the financial support from the National Natural Science Foundation of China (Nos. 42072160, 42272149, and 42472175) and Fundamental Research Funds for the Central Universities (YCX2021002). Rixin Zhao also thanks China Scholarship Council for financial support for a one-year visit to Durham University (No. 202206450073).

## AUTHOR DECLARATIONS

### Conflict of Interest

The authors have no conflicts to disclose.

## Author Contributions

**Rixin Zhao:** Data curation (equal); Formal analysis (equal); Investigation (equal); Methodology (equal); Software (equal); Visualization (equal); Writing – original draft (equal); Writing – review & editing (equal). **Haitao Xue:** Funding acquisition (equal); Project administration (equal); Supervision (equal). **Shuangfang Lu:** Supervision (equal). **H. Chris Greenwell:** Funding acquisition (equal); Supervision (equal); Writing – review & editing (equal). **Yaohui Xu:** Supervision (equal). **Taohua He:** Validation (equal). **Valentina Erastova:** Conceptualization (equal); Software (equal); Supervision (equal); Writing – review & editing (equal).

## DATA AVAILABILITY

The data that support the findings of this study are available within the article and its [supplementary material](#).

## REFERENCES

- <sup>1</sup>W. Zhao, S. Hu, L. Hou, T. Yang, X. Li, B. Guo, and Z. Yang, "Types and resource potential of continental shale oil in China and its boundary with tight oil," *Pet. Explor. Dev.* **47**(1), 1–11 (2020).
- <sup>2</sup>W. Zhao, C. Bian, Y. Li, J. Zhang, K. He, W. Liu, B. Zhang, Z. Lei, C. Liu, J. Zhang, M. Guan, and S. Liu, "Enrichment factors of movable hydrocarbons in lacustrine shale oil and exploration potential of shale oil in Gulong Sag, Songliao Basin, NE China," *Pet. Explor. Dev.* **50**(3), 520–533 (2023).

- <sup>3</sup>W. Li, J. Li, S. Lu, G. Chen, X. Pang, P. Zhang, and T. He, "Evaluation of gas-in-place content and gas-adsorbed ratio using carbon isotope fractionation model: A case study from Longmaxi shales in Sichuan Basin, China," *Int. J. Coal Geol.* **249**, 103881 (2022).
- <sup>4</sup>E. Wang, Y. Feng, T. Guo, and M. Li, "Oil content and resource quality evaluation methods for lacustrine shale: A review and a novel three-dimensional quality evaluation model," *Earth-Sci. Rev.* **232**, 104134 (2022).
- <sup>5</sup>Z.-Z. Lin, J.-Q. Li, S.-F. Lu, Q.-H. Hu, P.-F. Zhang, J.-J. Wang, Q. Zhi, H.-S. Huang, N. Yin, Y. Wang, and T.-C. Ge, "The occurrence characteristics of oil in shales matrix from organic geochemical screening data and pore structure properties: An experimental study," *Pet. Sci.* **21**, 1–13 (2023).
- <sup>6</sup>R. Zhao, H. Xue, S. Lu, J. Li, S. Tian, M. Wang, and Z. Dong, "Multi-scale pore structure characterization of lacustrine shale and its coupling relationship with material composition: An integrated study of multiple experiments," *Mar. Pet. Geol.* **140**, 105648 (2022).
- <sup>7</sup>B. Liu, H. Wang, X. Fu, Y. Bai, L. Bai, M. Jia, and B. He, "Lithofacies and depositional setting of a highly prospective lacustrine shale oil succession from the Upper Cretaceous Qingshankou Formation in the Gulong sag, northern Songliao Basin, northeast China," *Bulletin* **103**(2), 405–432 (2019).
- <sup>8</sup>Q. Tan, Y. Kang, L. You, F. Xu, and S. Meng, "A comprehensive insight into the multiscale pore structure characterization of saline-lacustrine tight carbonate reservoir," *J. Pet. Sci. Eng.* **187**, 106744 (2020).
- <sup>9</sup>C. Zou, X. Jin, R. Zhu, G. Gong, L. Sun, J. Dai, D. Meng, X. Wang, J. Li, S. Wu, X. Liu, J. Wu, and L. Jiang, "Do shale pore throats have a threshold diameter for oil storage?," *Sci. Rep.* **5**(1), 13619 (2015).
- <sup>10</sup>S. Luo, J. L. Lutkenhaus, and H. Nasrabadi, "Use of differential scanning calorimetry to study phase behavior of hydrocarbon mixtures in nano-scale porous media," *J. Pet. Sci. Eng.* **163**, 731–738 (2018).
- <sup>11</sup>Q. Yang, B. Jin, D. Banerjee, and H. Nasrabadi, "Direct visualization and molecular simulation of dewpoint pressure of a confined fluid in sub-10 nm slit pores," *Fuel* **235**, 1216–1223 (2019).
- <sup>12</sup>H. C. Greenwell, W. Jones, P. V. Coveney, and S. Stackhouse, "On the application of computer simulation techniques to anionic and cationic clays: A materials chemistry perspective," *J. Mater. Chem.* **16**(8), 708–723 (2006).
- <sup>13</sup>F. Xiong, Z. Jiang, P. Li, X. Wang, H. Bi, Y. Li, Z. Wang, M. A. Amooie, M. R. Soltanian, and J. Moortgat, "Pore structure of transitional shales in the Ordos Basin, NW China: Effects of composition on gas storage capacity," *Fuel* **206**, 504–515 (2017).
- <sup>14</sup>D. J. A. Williams and K. P. Williams, "Electrophoresis and zeta potential of kaolinite," *J. Colloid Interface Sci.* **65**(1), 79–87 (1978).
- <sup>15</sup>L. M. Wu, C. H. Zhou, J. Keeling, D. S. Tong, and W. H. Yu, "Towards an understanding of the role of clay minerals in crude oil formation, migration and accumulation," *Earth-Sci. Rev.* **115**(4), 373–386 (2012).
- <sup>16</sup>L. T. Ko, R. G. Loucks, T. Zhang, S. C. Ruppel, and D. Shao, "Pore and pore network evolution of Upper Cretaceous Boquillas (Eagle Ford-equivalent) mudrocks: Results from gold tube pyrolysis experiments," *Bulletin* **100**(11), 1693–1722 (2016).
- <sup>17</sup>S. P. Tan, X. Qiu, M. Dejam, and H. Adidharma, "Critical point of fluid confined in nanopores: Experimental detection and measurement," *J. Phys. Chem. C* **123**(15), 9824–9830 (2019).
- <sup>18</sup>G. Yang, Z. Fan, and X. Li, "Determination of confined fluid phase behavior using extended Peng-Robinson equation of state," *Chem. Eng. J.* **378**, 122032 (2019).
- <sup>19</sup>J. Cai, T. Jin, J. Kou, S. Zou, J. Xiao, and Q. Meng, "Lucas–Washburn equation-based modeling of capillary-driven flow in porous systems," *Langmuir* **37**(5), 1623–1636 (2021).
- <sup>20</sup>B. Coasne, C. Alba-Simionesco, F. Audonnet, G. Dosseh, and K. E. Gubbins, "Adsorption and structure of benzene on silica surfaces and in nanopores," *Langmuir* **25**(18), 10648–10659 (2009).
- <sup>21</sup>R. J. Ambrose, R. C. Hartman, M. Diaz-Campos, I. Y. Akkuttu, and C. H. Sondergeld, "Shale gas-in-place calculations. Part I: New pore-scale considerations," *SPE J.* **17**(1), 219–229 (2012).
- <sup>22</sup>P. A. Russo, M. M. L. Ribeiro Carrott, and P. J. M. Carrott, "Trends in the condensation/evaporation and adsorption enthalpies of volatile organic compounds on mesoporous silica materials," *Microporous Mesoporous Mater.* **151**, 223–230 (2012).
- <sup>23</sup>T. Pitakbunkate, P. B. Balbuena, G. J. Moridis, and T. A. Blasingame, "Effect of confinement on pressure/volume/temperature properties of hydrocarbons in shale reservoirs," *SPE J.* **21**(2), 621–634 (2016).
- <sup>24</sup>Y. Hamada, K. Koga, and H. Tanaka, "Phase equilibria and interfacial tension of fluids confined in narrow pores," *J. Chem. Phys.* **127**(8), 084908 (2007).
- <sup>25</sup>S. K. Singh, A. Sinha, G. Deo, and J. K. Singh, "Vapor–liquid phase coexistence, critical properties, and surface tension of confined alkanes," *J. Phys. Chem. C* **113**(17), 7170–7180 (2009).
- <sup>26</sup>T. Q. Vo and B. Kim, "Transport phenomena of water in molecular fluidic channels," *Sci. Rep.* **6**(1), 33881 (2016).
- <sup>27</sup>H. Sui, F. Zhang, Z. Wang, D. Wang, and Y. Wang, "Molecular simulations of oil adsorption and transport behavior in inorganic shale," *J. Mol. Liq.* **305**, 112745 (2020).
- <sup>28</sup>E. G. Derouane, "On the physical state of molecules in microporous solids," *Microporous Mesoporous Mater.* **104**(1–3), 46–51 (2007).
- <sup>29</sup>G. D. Barbosa, M. L. D'Lima, S. M. H. Daghash, M. Castier, F. W. Tavares, and L. Travalloni, "Cubic equations of state extended to confined fluids: New mixing rules and extension to spherical pores," *Chem. Eng. Sci.* **184**, 52–61 (2018).
- <sup>30</sup>Z. Song, Y. Song, J. Guo, Z. Zhang, and J. Hou, "Adsorption induced critical shifts of confined fluids in shale nanopores," *Chem. Eng. J.* **385**, 123837 (2020).
- <sup>31</sup>L. Travalloni, M. Castier, F. W. Tavares, and S. I. Sandler, "Thermodynamic modeling of confined fluids using an extension of the generalized van der Waals theory," *Chem. Eng. Sci.* **65**(10), 3088–3099 (2010).
- <sup>32</sup>X. Liu and D. Zhang, "A review of phase behavior simulation of hydrocarbons in confined space: Implications for shale oil and shale gas," *J. Nat. Gas Sci. Eng.* **68**, 102901 (2019).
- <sup>33</sup>J. Li, S. Wang, S. Lu, P. Zhang, J. Cai, J. Zhao, and W. Li, "Microdistribution and mobility of water in gas shale: A theoretical and experimental study," *Mar. Pet. Geol.* **102**, 496–507 (2019).
- <sup>34</sup>J. Cui and L. Cheng, "A theoretical study of the occurrence state of shale oil based on the pore sizes of mixed Gaussian distribution," *Fuel* **206**, 564–571 (2017).
- <sup>35</sup>J. Li, L. Shuangfang, C. Jianchao, Z. Pengfei, X. Haitao, and Z. Xuebo, "Adsorbed and free oil in lacustrine nanoporous shale: A theoretical model and a case study," *Energy Fuels* **32**(12), 12247–12258 (2018).
- <sup>36</sup>A. C. T. van Duin and S. R. Larter, "Molecular dynamics investigation into the adsorption of organic compounds on kaolinite surfaces," *Org. Geochem.* **32**(1), 143–150 (2001).
- <sup>37</sup>T. Underwood, V. Erastova, and H. C. Greenwell, "Wetting effects and molecular adsorption at hydrated kaolinite clay mineral surfaces," *J. Phys. Chem. C* **120**(21), 11433–11449 (2016).
- <sup>38</sup>Z. Cao, H. Jiang, J. Zeng, H. Saibi, T. Lu, X. Xie, Y. Zhang, and G. Zhou, "Nanoscale liquid hydrocarbon adsorption on clay minerals: A molecular dynamics simulation of shale oils," *Chem. Eng. J.* **420**, 127578 (2020).
- <sup>39</sup>X. Dong, W. Xu, R. Liu, Z. Chen, N. Lu, and W. Guo, "Insights into adsorption and diffusion behavior of shale oil in slit nanopores: A molecular dynamics simulation study," *J. Mol. Liq.* **359**, 119322 (2022).
- <sup>40</sup>R. Zhao, H. Xue, S. Lu, H. C. Greenwell, and V. Erastova, "Revealing crucial effects of reservoir environment and hydrocarbon fractions on fluid behaviour in kaolinite pores," *Chem. Eng. J.* **489**, 151362 (2024).
- <sup>41</sup>S. Wang, Q. Feng, F. Javadpour, T. Xia, and Z. Li, "Oil adsorption in shale nanopores and its effect on recoverable oil-in-place," *Int. J. Coal Geol.* **147–148**, 9–24 (2015).
- <sup>42</sup>H. Xiong, D. Devegowda, and L. Huang, "Water bridges in clay nanopores: Mechanisms of formation and impact on hydrocarbon transport," *Langmuir* **36**(3), 723–733 (2020).
- <sup>43</sup>S. Sanyal, U. K. Bhui, D. Balaga, and S. S. Kumar, "Interaction study of montmorillonite-crude oil-brine: Molecular-level implications on enhanced oil recovery during low saline water flooding from hydrocarbon reservoirs," *Fuel* **254**, 115725 (2019).
- <sup>44</sup>L. Zhang, X. Lu, X. Liu, Q. Li, Y. Cheng, Q. Hou, and J. Cai, "Distribution and mobility of crude oil–brine in clay mesopores: Insights from molecular dynamics simulations," *Langmuir* **35**(46), 14818–14832 (2019).
- <sup>45</sup>M. Wang, H. Xue, S. Tian, R. W. T. Wilkins, and Z. Wang, "Fractal characteristics of Upper Cretaceous lacustrine shale from the Songliao Basin, NE China," *Mar. Pet. Geol.* **67**, 144–153 (2015).

- <sup>46</sup>P. Zhang, S. Lu, J. Li, H. Xue, W. Li, and P. Zhang, "Characterization of shale pore system: A case study of Paleogene Xin'gouzui formation in the Jiangnan basin, China," *Mar. Pet. Geol.* **79**, 321–334 (2017).
- <sup>47</sup>X. Song and J. K. Chen, "A comparative study on Poiseuille flow of simple fluids through cylindrical and slit-like nanochannels," *Int. J. Heat Mass Transfer* **51**(7), 1770–1779 (2008).
- <sup>48</sup>S. Wang, Z. H. A. Ming, L. U. Shuangfang, Q. I. N. Yong, X. I. A. Tian, and C. Zhang, "Molecular dynamics simulation of liquid alkane occurrence state in pores and slits of shale organic matter," *Pet. Explor. Dev.* **42**(6), 844–851 (2015).
- <sup>49</sup>S. Tian, V. Erastova, S. Lu, H. C. Greenwell, T. R. Underwood, H. Xue, F. Zeng, G. Chen, C. Wu, and R. Zhao, "Understanding model crude oil component interactions on kaolinite silicate and aluminol surfaces: Toward improved understanding of shale oil recovery," *Energy Fuels* **32**(2), 1155–1165 (2018).
- <sup>50</sup>S. Wang, F. Javadpour, and Q. Feng, "Molecular dynamics simulations of oil transport through inorganic nanopores in shale," *Fuel* **171**, 74–86 (2016).
- <sup>51</sup>J. Chen, F. Wang, H. Liu, and H. Wu, "Molecular mechanism of adsorption/desorption hysteresis: Dynamics of shale gas in nanopores," *Sci. China: Phys., Mech. Astron.* **60**(1), 014611 (2017).
- <sup>52</sup>G. Chen, S. Lu, J. Zhang, Q. Xue, T. Han, H. Xue, S. Tian, J. Li, C. Xu, and M. Pervukhina, "Keys to linking GCMC simulations and shale gas adsorption experiments," *Fuel* **199**, 14–21 (2017).
- <sup>53</sup>R. G. Loucks, R. M. Reed, S. C. Ruppel, and U. Hammes, "Spectrum of pore types and networks in mudrocks and a descriptive classification for matrix-related mudrock pores," *Bulletin* **96**(6), 1071–1098 (2012).
- <sup>54</sup>Y. Wu, P. Tahmasebi, C. Lin, and C. Dong, "Process-based and dynamic 2D modeling of shale samples: Considering the geology and pore-system evolution," *Int. J. Coal Geol.* **218**, 103368 (2020).
- <sup>55</sup>L. T. Ko, R. G. Loucks, S. C. Ruppel, T. Zhang, and S. Peng, "Origin and characterization of Eagle Ford pore networks in the south Texas Upper Cretaceous shelf," *Bulletin* **101**(3), 387–418 (2017).
- <sup>56</sup>R. T. Downs and M. Hall-Wallace, "The American Mineralogist crystal structure database," *Am. Min.* **88**(1), 247–250 (2003).
- <sup>57</sup>P. V. Brady, R. T. Cygan, and K. L. Nagy, "Molecular controls on kaolinite surface charge," *J. Colloid Interface Sci.* **183**(2), 356–364 (1996).
- <sup>58</sup>B. K. Schroth and G. Sposito, "Surface charge properties of kaolinite," *Clays Clay Miner.* **45**, 85–91 (1997).
- <sup>59</sup>E. Tombácz and M. Szekeres, "Surface charge heterogeneity of kaolinite in aqueous suspension in comparison with montmorillonite," *Appl. Clay Sci.* **34**(1–4), 105–124 (2006).
- <sup>60</sup>W. Humphrey, A. Dalke, and K. Schulten, "VMD: Visual molecular dynamics," *J. Mol. Graph.* **14**(1), 33–38 (1996).
- <sup>61</sup>W. Zhang, Q. Feng, S. Wang, and X. Xing, "Oil diffusion in shale nanopores: Insight of molecular dynamics simulation," *J. Mol. Liq.* **290**, 111183 (2019).
- <sup>62</sup>M. S. Santos, L. F. M. Franco, M. Castier, and I. G. Economou, "Molecular dynamics simulation of n-alkanes and CO<sub>2</sub> confined by calcite nanopores," *Energy Fuels* **32**(2), 1934–1941 (2018).
- <sup>63</sup>D. D. Do and H. D. Do, "Adsorption of flexible n-alkane on graphitized thermal carbon black: Analysis of adsorption isotherm by means of GCMC simulation," *Chem. Eng. Sci.* **60**(7), 1977–1986 (2005).
- <sup>64</sup>H. J. C. Berendsen, D. van der Spoel, and R. van Drunen, "GROMACS: A message-passing parallel molecular dynamics implementation," *Comput. Phys. Commun.* **91**(1–3), 43–56 (1995).
- <sup>65</sup>M. J. Abraham, T. Murtola, R. Schulz, S. Páll, J. C. Smith, B. Hess, and E. Lindahl, "GROMACS: High performance molecular simulations through multi-level parallelism from laptops to supercomputers," *SoftwareX* **1–2**, 19–25 (2015).
- <sup>66</sup>K. Vanommeslaeghe, E. Hatcher, C. Acharya, S. Kundu, S. Zhong, J. Shim, E. Darian, O. Guvench, P. Lopes, I. Vorobyov, and A. D. MacKerell, "CHARMM General Force Field (CGenFF): A force field for drug-like molecules compatible with the CHARMM all-atom additive biological force fields," *J. Comput. Chem.* **31**(4), 671–690 (2010).
- <sup>67</sup>R. T. Cygan, J.-J. Liang, and A. G. Kalinichev, "Molecular models of hydroxide, oxyhydroxide, and clay phases and the development of a general force field," *J. Phys. Chem. B* **108**(4), 1255–1266 (2004).
- <sup>68</sup>P. Bjelkmar, P. Larsson, M. A. Cuendet, B. Hess, and E. Lindahl, "Implementation of the CHARMM Force Field in GROMACS: Analysis of protein stability effects from correction maps, virtual interaction sites, and water models," *J. Chem. Theory Comput.* **6**(2), 459–466 (2010).
- <sup>69</sup>R. W. Pastor and A. D. MacKerell, "Development of the CHARMM force field for lipids," *J. Phys. Chem. Lett.* **2**(13), 1526–1532 (2011).
- <sup>70</sup>L. B. Wright and T. R. Walsh, "First-principles molecular dynamics simulations of NH<sub>4</sub><sup>+</sup> and CH<sub>3</sub>COO<sup>-</sup> adsorption at the aqueous quartz interface," *J. Chem. Phys.* **137**(22), 224702 (2012).
- <sup>71</sup>A. A. Skelton, P. Fenter, J. D. Kubicki, D. J. Wesolowski, and P. T. Cummings, "Simulations of the quartz(1011)/water interface: A comparison of classical force fields, ab initio molecular dynamics, and x-ray reflectivity experiments," *J. Phys. Chem. C* **115**(5), 2076–2088 (2011).
- <sup>72</sup>NIST, *National Institute of Standards and Technology (NIST) Chemistry WebBook* (NIST, 2009).
- <sup>73</sup>*CRC Handbook of Chemistry and Physics*, 97th ed., edited by W. M. Haynes (CRC Press, Boca Raton, 2016).